THE ASTROPHYSICAL JOURNAL, 293:132–147, 1985 June 1

BUBBLES AND JETS IN THE CENTER OF M51

HOLLAND C. FORD[1,2]
Space Telescope Science Institute; and Department of Physics and Astronomy, The John Hopkins University

PATRICK C. CRANE
National Radio Astronomy Observatory[3]

GEORGE H. JACOBY
Kitt Peak National Observatory

DAVID G. LAWRIE[2]
Ohio State University

AND

JAN MATHIJS VAN DER HULST
Netherlands Foundation for Radio Astronomy
Received 1984 August 20; accepted 1984 December 17

ABSTRACT

We present monochromatic Hα + [N II] pictures and high-resolution VLA 20 cm and 6 cm radio maps which show a bright, filled cloud and a large ring paired across the nucleus of M51. The 20 cm radio map shows that the southern cloud has a bright, bow-shaped region on its leading edge, suggesting that we are observing a working surface. The optical pictures and radio maps partially resolve the nucleus and show that it is elongated in the direction of the cloud and ring. Low-resolution spectrophotometry reveals that the cloud has strong [O I], [O II], [N I], [N II], and [S II] emission, with line ratios similar to the shock-excited gas in some supernova remnants. High-dispersion spatially resolved spectra show that the velocity dispersion in the cloud is larger than in the nucleus, with a 2000 km s^{-1} full width at zero intensity, and that the line broadening and line ratios change abruptly at the edges of the ring and cloud. We use the optical and radio data to derive the sizes, ages, masses, filling factors, and minimum energies of the ring, nucleus, and cloud. The ring and cloud exceed galactic supernova remnants with respect to these quantities by factors of 100 to 1000. In view of the morphologies, mass motions, radio characteristics, spectroscopic similarities to supernova remnants, and abrupt transitions from the ring and cloud to the disk, we conclude that the gas in these structures is excited in shocks rather than photoionized by a nonstellar source in the nucleus. We use shock-front models to show that the N/H and N/O ratios are extraordinarily high in M51's nuclear disk. We emphasize that the primary sites of nuclear activity in M51, as measured by optical and radio luminosity and by forbidden-line widths, are *outside* the nucleus. We conclude that the nuclear phenomena are the result of an active nucleus which has created a pair of bubbles in the disk. The bubbles may have their origin in a bidirectional jet emanating from the nucleus. The jet interacts with the disk of M51 and, through entrainment and compression of the gas in the disk, creates shocks which give rise to the emission, and, by heating the gas, inflates bubbles in the disk. Alternatively, the bubbles may be ejected from the nucleus as discrete entities. Our observations strengthen earlier characterizations of M51 as Seyfert-like and give a clear optical and radio example of at least one way that an active nucleus can produce a narrow forbidden-line region.

Subject headings: galaxies: individual — galaxies: jets — galaxies: nuclei — radio sources: galaxies

I. INTRODUCTION

Active galaxies vary from highly luminous quasars to spirals with barely detectable nuclear activity. In spite of the diverse characteristics of quasars, BL Lac objects, radio ellipticals, Seyferts, and active spirals, many authors have suggested that there is a continuity of properties between classes of active galaxies (e.g., Sandage 1971). There is a growing belief that all such phenomena have an origin in events occurring around central, massive black holes. In this view, the level and characteristics of nuclear activity are governed by fueling rate (Norman and Silk 1983) and galactic environment (Blandford and Rees 1974). A recent series of papers (Wilson and Willis 1980; Ulvestad, Wilson, and Sramek 1981; Ulvestad and Wilson 1983) strengthens these ideas by showing that many type 2 Seyfert galaxies have central double and triple radio sources which appear to be weak, small-scale analogs of the large-scale structures seen in powerful radio galaxies. Wilson and Ulvestad (1982, hereafter WU; 1983) conclude that the radio sources in NGC 1068 and NGC 4151 are interacting with gas near the nuclei, and show that the radio structures can be explained by ram-pressure bending of stationary jets.

M51, which is at the low end of the scale of nuclear activity, has a relatively weak, elongated nonthermal nuclear radio source (Spencer and Burke 1972; Segalovitz 1976; Hummel 1980) and optical emission which deviates from circular

[1] Visiting Fellow, Australian National University, Stromlo and Siding Spring Observatories.

[2] Visiting Astronomer, Kitt Peak National Observatory, which is operated by the Association of Universities for Research in Astronomy, Inc., under contract with the National Science Foundation.

[3] Operated by Associated Universities, Inc., under contract with the National Science Foundation.

motion near the nucleus (Burbidge and Burbidge 1964). Goad, De Veny, and Goad (1979, herafter GDVG) confirmed the noncircular motions found by the Burbidges and showed that the emission lines are broadened by a few hundred km s^{-1} in and near the nucleus. Rose and Searle (1982, hereafter RS) investigated photoionization in M51 and concluded that the nucleus and surrounding gas are photoionized by a central nonthermal continuum. Their characterization of M51 as Seyfert-like was strengthened by Rose and Cecil (1983, hereafter RC), who found that the nuclear permitted and forbidden lines have broad asymmetrical wings with full widths at zero intensity ~ 1800 km s^{-1}.

In this paper we present optical and radio observations which clarify the nature of the nuclear activity by showing that M51 appears to have a bidirectional jet which emanates from the nucleus and interacts with the surrounding interstellar medium. In § II we present the observational basis for our conclusions. These include Hα + [N II] monochromatic photographs and VLA 20 cm and 6 cm radio maps which reveal a bright, resolved cloud and an extraordinary ring paired across the nucleus. Our spectrophotometry shows that the nuclear emission-line characteristics change abruptly at the edges of the ring and the cloud, and that the cloud has internal velocities larger than the nucleus and a spectrum similar to some galactic supernova remnants. In § III we derive the physical characteristics of the nuclear emission regions and then use these to discuss the ionization and excitation of the ring and cloud. Finally, we present the arguments which lead us to the conclusion that these features have their origin in a jet flowing from the nucleus. Section IV summarizes our observations and conclusions.

II. OBSERVATIONS

a) Optical and Radio Images

A short exposure Hα + [N II] image-tube photograph of M51 taken with the Shane 3 m telescope through thin cirrus and during excellent seeing revealed a bright emission line cloud 3″ south and 0″.3 east of the nucleus. Subsequent spectrophotometry and Hα + [N II] images taken with the video camera on the KPNO 2.1 m telescope and with an RCA CCD on the KPNO No. 1 0.9 m telescope confirmed the reality of the extra nuclear cloud (XNC). Both the video camera and CCD pictures revealed a new emission feature, a large-diameter ring ($d \approx 9''$ = 420 pc at D = 9.6 Mpc; Sandage and Tamman 1974) centered $\sim 9''$ northwest of the nucleus on the line joining the nucleus and the center of the XNC. Figure 1 (Plate 15) shows the Hα + [N II] CCD picture with two windowings; the first shows the nucleus and XNC, and the second shows the somewhat inconspicuous ring. All photographs show that the XNC is resolved and has a peak surface brightness at the center, which suggests that its morphology is closer to a filled sphere than to a shell. The nucleus is clearly elongated in the direction of the ring and XNC in all our emission-line pictures, having a ratio of minor to major axis of ~ 0.75. The positions of the XNC and ring relative to the nucleus (the directions north and east are positive) are given in Table 1, along with a journal of the observations. The optical positions of the XNC derived from the pictures are in excellent agreement. The position of the ring and its outside diameter could not be measured with the same precision as the position of the XNC.

We observed M51 at 6 cm on 1982 August 15 with the Very Large Array in the B configuration and at 20 cm on 1983 August 26 in the A configuration. During each 6 hr observation, we switched between M51 and the nearby phase calibrator 1418+546, which had flux densities of 2.26 Jy and 1.06 Jy respectively during the two observations, measured relative to the primary flux-density calibrator 3C 286 (Baars *et al.* 1977). At 6 cm we observed with a 50 MHz bandwidth centered at 4885.1 MHz. Because of instrumental improvements, we observed at 20 cm with two 50 MHz bandwidths centered at 1464.9 and 1514.9 MHz. The instrumental phases at 6 cm were adjusted using the self-calibration algorithm (Schwab 1980). Observations taken in the smaller configurations (van der Hulst *et al.* 1985) were added to provide information on the large-scale structure in M51.

Our high-resolution (1″) map of the total intensity at 20 cm is presented as a radiograph in Figure 2 (Plate 16) and as a contour plot in Figure 3. The transfer functions for Figures 2*a* and 2*b* were adjusted to emphasize the structures of the southern and northern sources respectively. The high-resolution 20 cm map shows that the XNC is limb-brightened in a bow-shaped region, which suggests that we are seeing either the working surface of a jet which emanates from the nucleus, or the interaction of a plasmoid ejected from the nucleus with the surrounding interstellar medium. When adjusted to show details in the northern ring (Fig. 2*b*), several "hot spots" appear. These hot spots and limb brightening on the NE edge occur where the ring is adjacent to (or overlaps) one of M51's inner spiral arms. This is but one of several arguments which we will use to conclude that the ring and XNC are in the disk of M51. The "ring" is probably a complete shell which appears as a ring because of projection; comparison of the brightness of the ring to that in the center suggests that the thickness of the shell is about 10% of its diameter.

The high-resolution (1″) map of the total intensity at 6 cm is presented as a radiograph in Figure 4 (Plate 17) and as a contour plot in Figure 5. Although the sensitivity is worse than for the corresponding 20 cm map, the two maps are in excellent agreement. The observed radio properties of the two sources and the nucleus are given in Table 2; those for the ring were estimated, while those for the nucleus and XNC were determined by fitting Gaussians. The spectral index of the XNC

TABLE 1

OPTICAL IMAGES OF M51

Date	Telescope	Focal Ratio (f)	Instrument	Filter	Exposure Time (minutes)	XNC x	XNC y	Ring x	Ring y	Ring Diameter
1973 May 3	Shane 3 m	5	Image intensifier	6570/50	3.5	0″.34	−3″.24	...	...	...
1979 Feb 19	KPNO 2.1 m	7.5	Video camera	5520/220	15.0	...	...	...	...	...
1979 Feb 19	KPNO 2.1 m	7.5	Video camera	5021/54	15.0	...	...	...	...	...
1979 Feb 19	KPNO 2.1 m	7.5	Video camera	6564/27	15.0	0″.40	−3″.10	...	...	...
1983 Jan 14	KPNO 0.9 m	13.5	RCA CCD	6563/38	30.0	0″.45	−3″.03	−0″.8	7″.8	8″.8

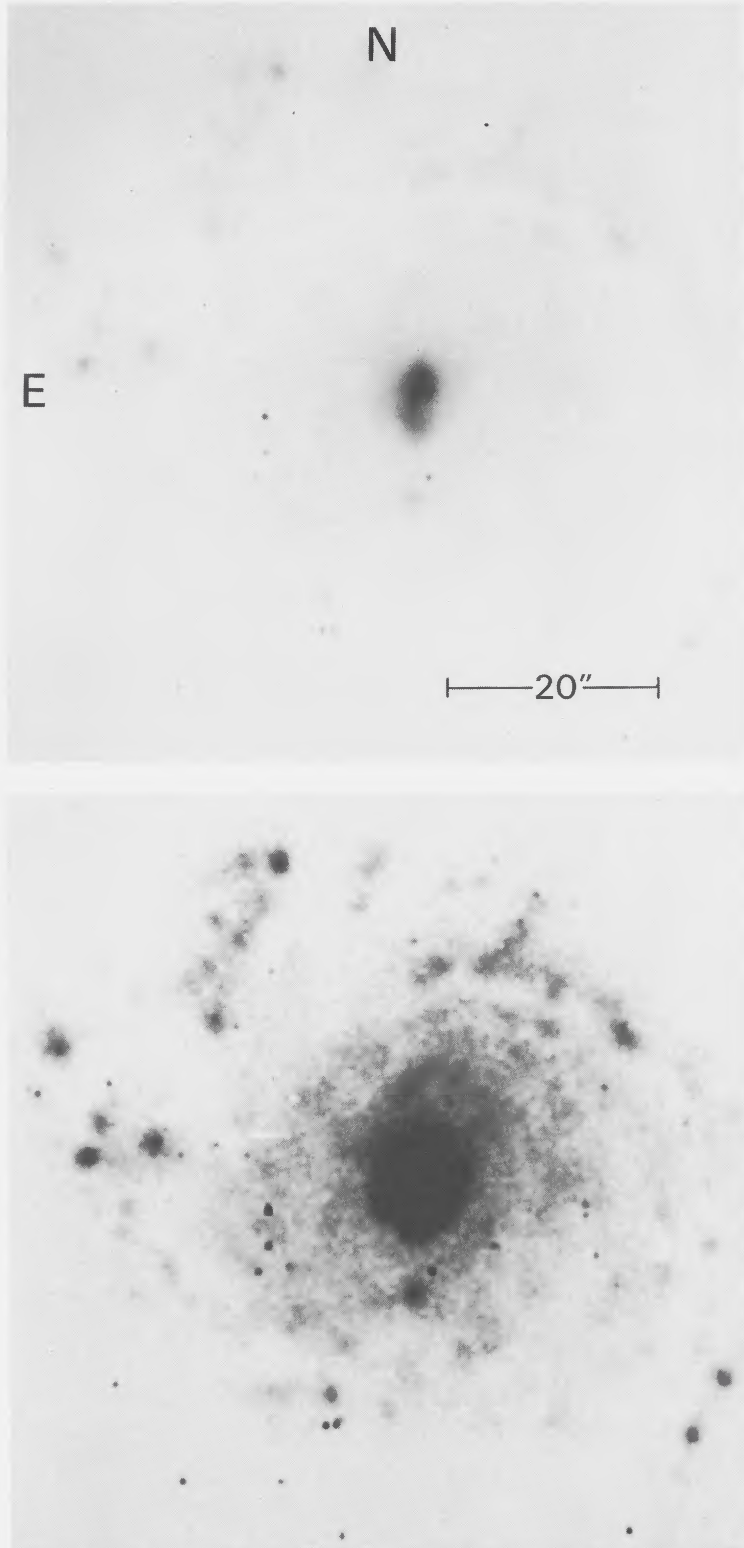

FIG. 1.—A 30 minute RCA CCD picture of M51 taken through a 6563/38 interference filter at the f/7.5 Cassegrain focus of the KPNO No. 1 0.9 m telescope. The upper panel, which is windowed to show high-surface-brightness detail near the nucleus, shows an elongated nucleus and a bright cloud $\sim 3\rlap{.}''5$ southeast of the nucleus along the direction of nuclear elongation. The lower panel is the same picture windowed to show low-surface-brightness detail. In addition to bright H II regions and diffuse emission in the disk, a large-diameter ring ($d \approx 9''$) can be seen centered $\sim 9''$ northwest of the nucleus.

FORD *et al.* (*see* page 133)

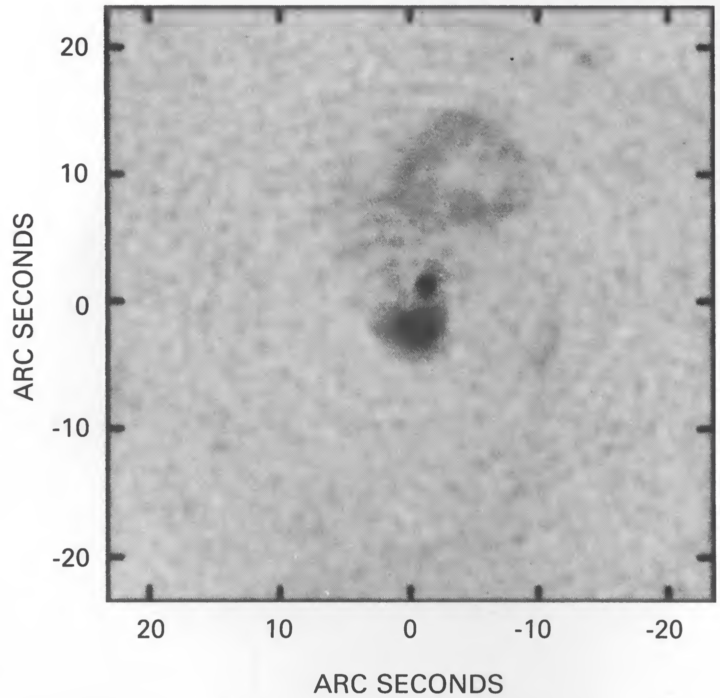

FIG. 2*a*.—Radiograph of the map of the total intensity at 20 cm, with 1″ resolution, of the nuclear region of M51. The transfer function has been adjusted to emphasize the structure in the southern cloud. Note the bright bow-shaped structure on the southeast edge.

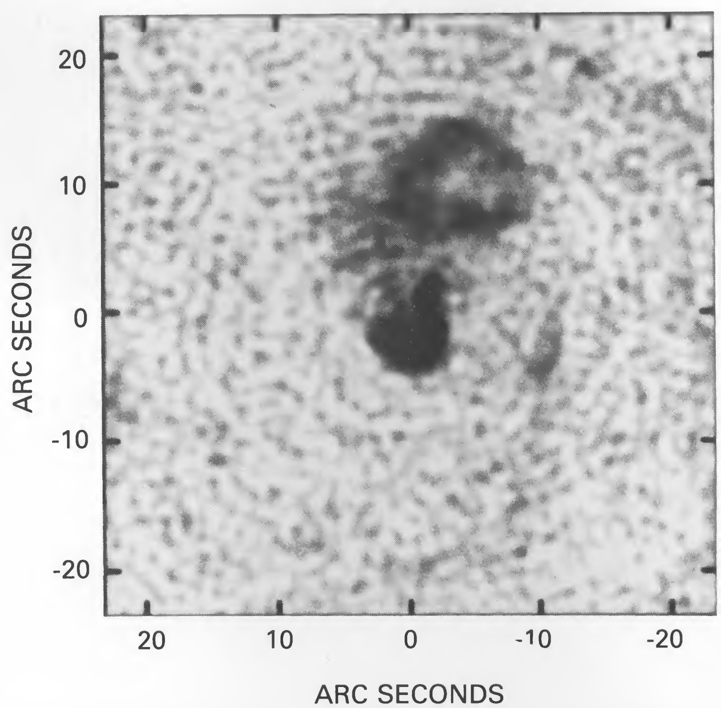

FIG. 2*b*.—The same map adjusted to emphasize the structure of the northern source. Note the elongated nucleus and the ring structure with hot spots or limb brightening on the northeast side.

FORD *et al.* (*see* page 133)

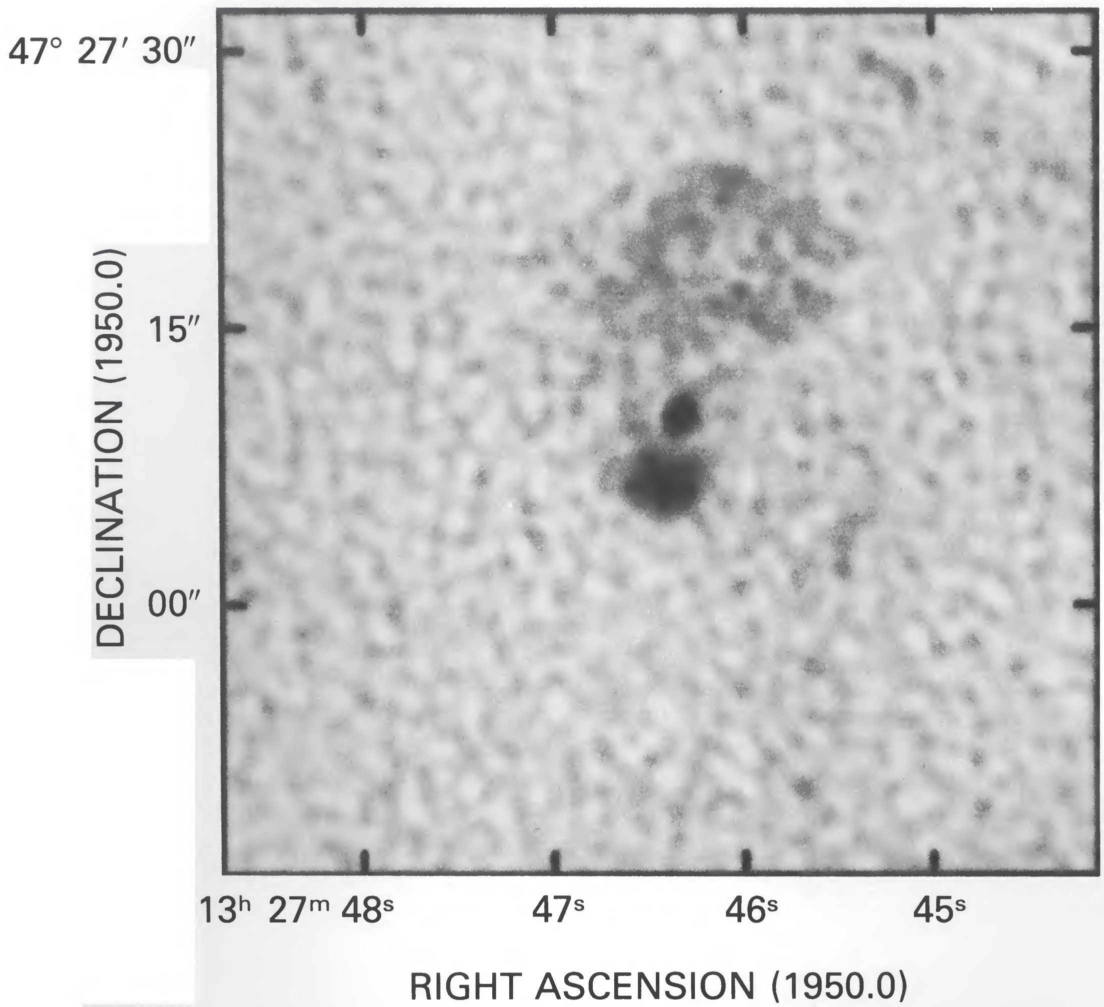

FIG. 4.—A radiograph of the map of the total intensity at 6 cm, with 1″ resolution, of the nuclear region of M51

FORD *et al.* (*see* page 133)

1985ApJ...293..132F

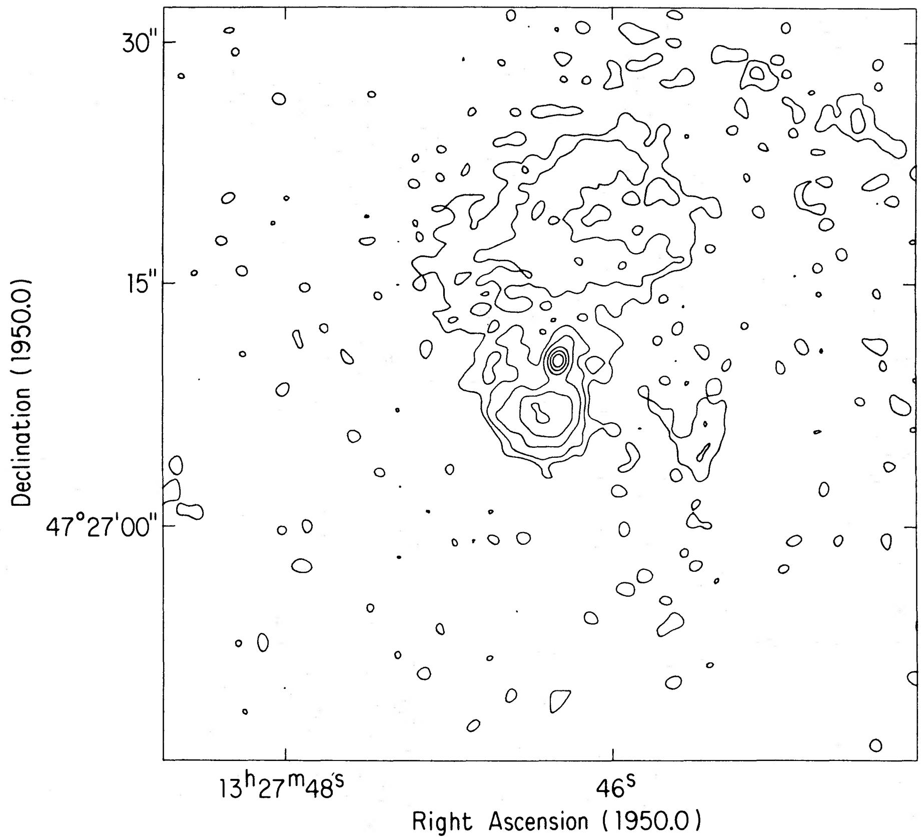

FIG. 3.—A contour plot of the map of the total intensity at 20 cm, with 1" resolution, of the nuclear region of M51. The contour levels are −5%, 5%, 10%, 20%, 40%, 60%, 80%, and 100% of the peak brightness of 2.12 mJy per beam.

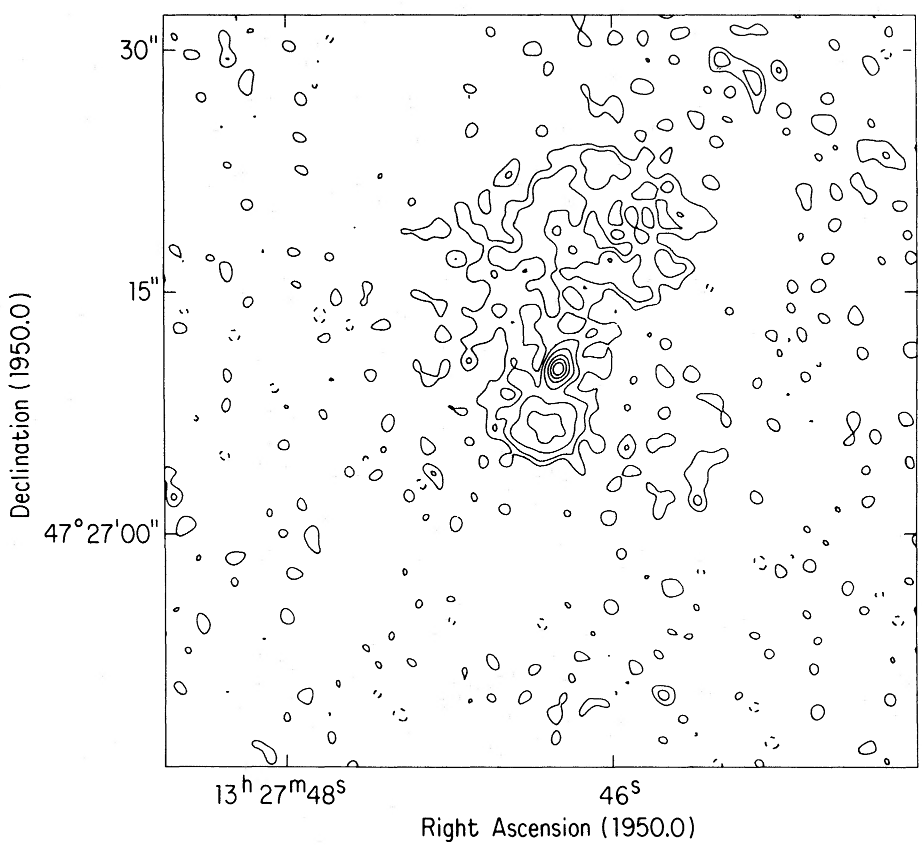

FIG. 5.—A contour plot of the map of the total intensity at 6 cm, with 1" resolution, of the nuclear region of M51. The contour levels are −5%, 5%, 10%, 20%, 40%, 60%, 80%, and 100% of the peak brightness of 1.00 mJy per beam.

TABLE 2

OBSERVED PROPERTIES OF THE NUCLEAR RADIO SOURCES IN M51[a]

PROPERTY	RING	NUCLEUS	XNC
Right ascension (1950.0)	$13^h27^m46^s.10$	$13^h27^m46^s.327$ ($0^s.003$)	$13^h27^m46^s.411$ ($0^s.026$)
Declination (1950.0)	47°27′18″.9	47°27′10″.25 (0″.04)	47°27′06″.78 (0″.19)
S(1465) (mJy)	26 (3)	3.59 (0.34)	14.85 (0.76)
S(4885) (mJy)	10 (1)	1.65 (0.14)	4.62 (0.26)
Spectral index	−0.8	−0.67	−1.0
Major axis	11″.6	1″.08 (0″.06)	2″.87 (0″.24)
Minor axis	8″.7	0″.53 (0″.12)	2″.15 (0″.14)
Position angle	98°	163° (7°)	112° (27°)

[a] Estimated uncertainties in parentheses.

(−1.0) is an average over the source; the observed values decrease from −0.7 at the bright bow-shaped region on the southeast edge to −1.4 at the northwest edge. A close correspondence between the radio and optical features is evident, although the peak radio brightness in the XNC is ∼0″.7 farther southeast than the peak optical emission. This apparent displacement may arise from the lower resolution of the optical pictures and confusion with the wings of the nuclear emission.

Figures 2 through 5 show that the nucleus is elongated along the direction of the ring and XNC, as is also seen in the optical pictures. The axial ratio is 0.5, somewhat more elongated than when measured optically (0.75).

These figures also show low-surface-brightness, diametrically opposed "spurs" orthogonal to the line joining the ring and XNC. The low-resolution (5″) maps of the total and polarized intensities at 6 cm, shown as contour plots in Figure 6, reveal that the "spurs" connect with other low-surface-brightness blobs to form the innermost extensions of M51's spiral arms. The peak polarized emission associated with the ring is 25%; the corresponding upper limit at 20 cm is 8%.

b) Spectrophotometry

We observed M51's nucleus and extranuclear cloud with the image-tube scanner (ITS) (Robinson and Wampler 1972, 1973) on Lick Observatory's Shane 3 m telescope, and with an intensified Texas Instruments 800 × 800 CCD (ICCD) on Kitt Peak's Mayall 4 m telescope. Details of the observations are recorded in Table 3. The Lick observations were made during good seeing (∼1″) with a 2″ × 2″ aperture centered on the nucleus and then on the southern cloud. The spectra spanned 3600 Å to 6800 Å in two grating settings, with 8 Å resolution, and were reduced to relative intensity versus linear wavelength with standard techniques (e.g., Jenner, Ford, and Jacoby 1979). We compared our reduced nuclear continuum relative intensities to Turnrose's (1976) multichannel spectrometer (Oke 1969) scans of M51's nucleus (7″ aperture), and found satisfactory agreement (±10%) between 4500 and 7000 Å. The comparison shows an apparent systematic error in our data below 4500 Å; consequently, we discarded the violet and ultraviolet ITS data. Mike Shara kindly took spectra for us of the nucleus and XNC using the KPNO Intensified Image Dissector Scanner (IIDS) on the Kitt Peak 2.1 m telescope with a 300 lines mm^{-1} grating and a 3″.4 diameter aperture. The IIDS spectra cover 3500–7000 Å and have relative and absolute line intensities for [O III] λ5007 and [N II] + Hα which are in good agreement with the Lick ITS data. We scaled the IIDS measurements of the [O II] λ3727 doublet to the ITS line intensities by multiplying the observed ITS [O III] λ5007 intensity by the IIDS ratio of [O II] λ3727 to [O III] λ5007, obtaining the [O II] values given in columns (2) and (3) of Table 4.

TABLE 3

JOURNAL OF SPECTROPHOTOMETRIC OBSERVATIONS

Position	Date	Integration Time (minutes)	Grooves (mm^{-1})	Blaze (Å)	Order	λ Central (Å)	λ Range (Å)	Reciprocal Dispersion (Å mm^{-1})	FWHM (Å)	Seeing
					Lick ITS					
Nucleus	1973 Jun 26	16	600	5000	1st	6455	2395	154	8	...
XNC[a]	1973 Jun 26	16	600	5000	1st	6455	2395	154	8	...
Nucleus	1973 Jun 28	16	600	5000	1st	4650	2020	154	8	...
XNC[a]	1973 Jun 28	16	600	5000	1st	4650	2020	154	8	...
					KPNO ICCD					
Nucleus .... P.A. = 0°	1983 Apr 14	1200	1200	...	1st RG1 block	6617	555	46	2.2	2″
Nucleus .... P.A. = 0°	1983 Apr 14	1200	1200	...	1st RG1 block	6617	555	46	2.2	2″
Nucleus .... P.A. = 169°	1983 Apr 15	2400	1200	...	1st RG1 block	6617	555	46	2.2	1″.5
Nucleus .... P.A. = 169°	1983 Apr 15	2700	1200	...	2nd $CuSO_4$	3745	275	23	1.2	1″.5
Nucleus .... P.A. = 0°	1983 Apr 15	2700	1200	...	2nd $CuSO_4$	3745	275	23	1.2	1″.5

[a] 3″ south of nucleus.

1985ApJ...293..132F

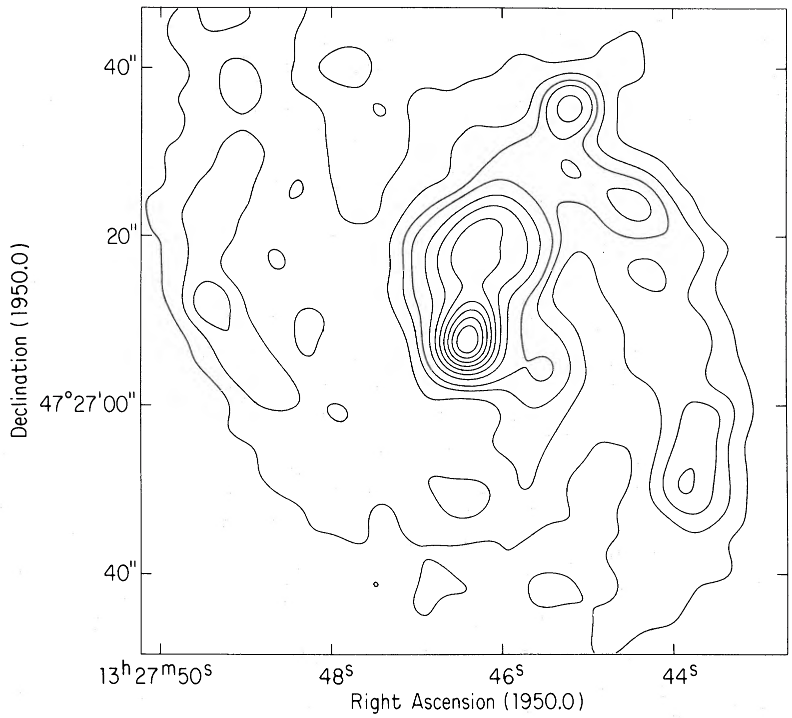

FIG. 6a

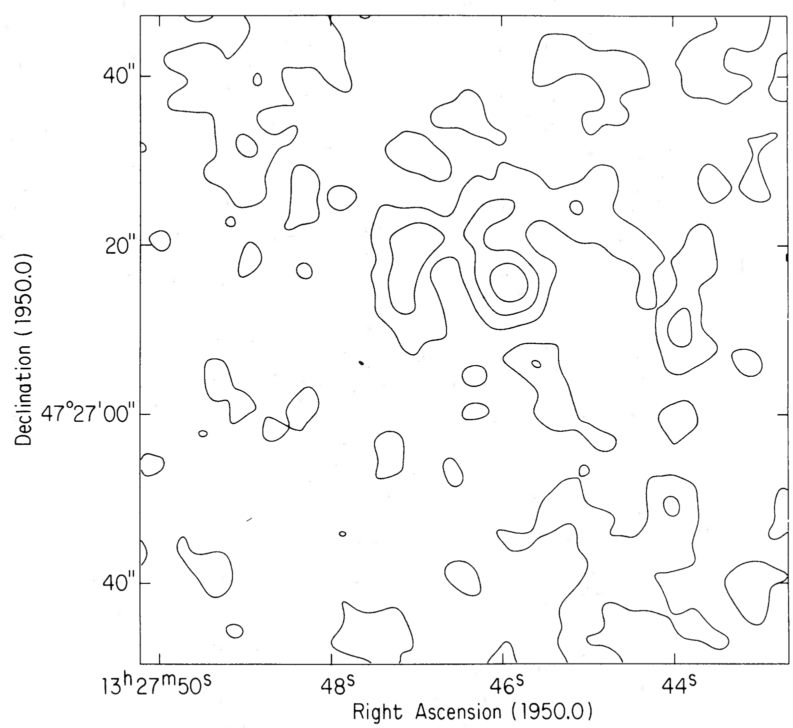

FIG. 6b

FIG. 6.—(*a*) Contour plot of the map of the total intensity at 6 cm, with 5″ resolution, of the nuclear region of M51. The contour levels are −5%, 5%, 10%, 20%, 30%, 40%, 50%, 60%, 70%, 80%, 90%, and 100% of the peak brightness of 4.69 mJy beam. Note the prominent inner spiral arms. (*b*) Contour plot of the map of the polarized intensity at 6 cm, with 5″ resolution, of the nuclear region of M51. The contour levels are 25%, 50%, 75%, and 100% of the peak brightness of 0.25 mJy per beam. The peak polarized emission is associated with the northern ring and corresponds to 25% linear polarization. Also, the inner spiral arms show significant linear polarization.

TABLE 4

EMISSION LINE INTENSITIES IN M51[a]

IDENTIFICATION (1)	OBSERVED LINE INTENSITIES: ITS XNC (2)	ITS Nucleus (3)	SIT[b] Nucleus (0°) (4)	SIT[b] Nucleus (90°) (5)	IRET[c] Nucleus (6)	DEREDDENED ITS XNC (7)	DEREDDENED ITS Nucleus (8)
[O II] λ3727	1.92[d]	1.28[d]	...	0.17	0.58	3.63	2.46
H I + He I λ3889	...	...	...	...	0.14	...	...
[S II] λ4068	...	...	...	...	0.04	...	...
[O III] λ4363	...	...	...	...	<0.02	...	...
H I λ4861	0.27	...	...	...	...	0.38	...
[O III] λ4959	0.37	0.63	0.63	0.32	0.39	0.51	0.86
[O III] λ5007	0.62	1.71	1.83	1.08	1.16	0.84	2.31
[N I] λ5200	0.34	≤0.11	...	...	...	0.44	≤0.14
[N II] λ5755	0.28	...	...	...	...	0.32	...
[O I] λ6300	0.42	...	0.22	0.23	0.13	0.44	...
[N II] λ6548	1.50	1.17	1.34	1.26	0.89	1.50	1.17
H I λ6563	1.00	1.00	1.00	1.00	1.00	1.00	1.00
[N II] λ6584	4.66	3.79	3.60	3.44	3.23	4.65	3.78
[S II] λ6716	0.73	0.55	0.65	0.70	0.48	0.71	0.54
[S II] λ6731	0.65	0.56	1.07	0.67	0.52	0.63	0.55
Flux for unity line strength (10^{-15} ergs cm^{-2} s^{-1})	30	55	16	17	...	59	108
n_e([S II]) (cm^{-3})	370	640	...	490	800	...	...

[a] Aperture size: ITS, 2″ × 2″; SIT, 2″ × 4″.3; IRET, 5″.
[b] RS.
[c] RC.
[d] IIDS Measurements scaled to the ITS data.

The ITS scans of the nucleus and XNC are shown in Figure 7. Although the spectra of the nucleus and XNC are qualitatively similar, with strong emission from [N II] and [S II], the differences between them show that we were relatively successful in separating the nucleus and XNC. Two facts show that the XNC, which is clearly outside the nucleus, exhibits properties usually associated with active nuclei. First, the [N II]/Hα ratio peaks in the XNC rather than in the nucleus. Although we will show that N/H and N/O are very high in the XNC, which we attribute to previous enrichment of the nuclear interstellar medium by CNO burning in massive stars, it is plausible that these ratios are as high or higher in the nucleus, which most likely has undergone episodes of intense star formation. However, the strength of the [N II] lines seen in active galactic nuclei is not primarily an abundance effect, but rather the consequence of photoionization by a nonthermal continuum or ionization and excitation in shocks. This is demonstrated by inspection of Figures 8 and 9 (Plates 18 and 19), which show that the [N II] λ6584/Hα ratio reverses in the bright H II regions which fall along the slit immediately north of the ring and south of the XNC. The interstellar gas in the H II regions must have abundances similar to the ring and XNC; consequently, the strength of [N II] in the bright nuclear structures is the signature of nuclear activity. The second characteristic of active galactic nuclei is line broadening, and the blending of the [S II] lines and of the Hα + [N II] emission lines shows that the line broadening is larger in the XNC than in the nucleus. These conclusions are confirmed by the high-dispersion ICCD spectrophotometry presented in the following section.

One of the most significant characteristics of the XNC spectrum is the unmistakable presence of strong emission from [N I] λ5200, a blended doublet which is often seen in the spectra of supernova remnants. In contrast to the XNC, the nucleus shows little or no emission from [N I] λ5200. The XNC spectrum also has a relatively strong emission line at $\lambda_{\rm obs}$ = 5772 Å, which corresponds to λ_0 = 5763 Å in M51's rest frame. The line could be either the auroral transition [N II] λ5755 with an 8 Å wavelength error, or it could be improperly sky-subtracted Hg I 5770. The latter possibility is not compelling because of the absence of an equivalent feature from the other line in the Hg city glow doublet, Hg I 5790. Because the line at 5772 Å is approximately as strong as [N II] λ5755 predicted by the shock models discussed in the next section, we think it probably is [N II] λ5755.

The observed emission-line intensities which we derived from the ITS scans are listed in columns (2) and (3) in Table 4. In order to give some appreciation for systematic errors and variations in relative line intensities due to different spatial sampling, we have included data from RS's silicon-intensified target (SIT) long-slit spectrophotometry of the nucleus at 0° position angle (col. [4]) and 90° position angle (col. [5]). Data from RC's intensified Reticon (IRET) spectrophotometry is listed in column (6). The overall agreement of the relative line intensities is acceptable; with the exception of [O II] λ3727, the differences are probably due to different mixings in the apertures of physically distinct regions. The [O II] λ3727 line strengths deserve special note. RC derived the [O II] λ3727 intensity listed in Table 4 by using the nuclear continuum flux to scale the RS [O II] λ3727 SIT intensity to the IRET data. The errors in both scalings could be as large as a factor of 2. RS also noted problems with their ultraviolet calibration and concluded they had a 50% uncertainty in their blue-to-red scaling. Because of possible problems in the SIT and IRET [O II] λ3727 line intensities, we will use the IIDS [O II] λ3727 intensities as scaled to the ITS data.

RS used the observed Balmer decrement in an H II region 11″ south of the nucleus to derive E_{B-V} = 0.32. We adopted

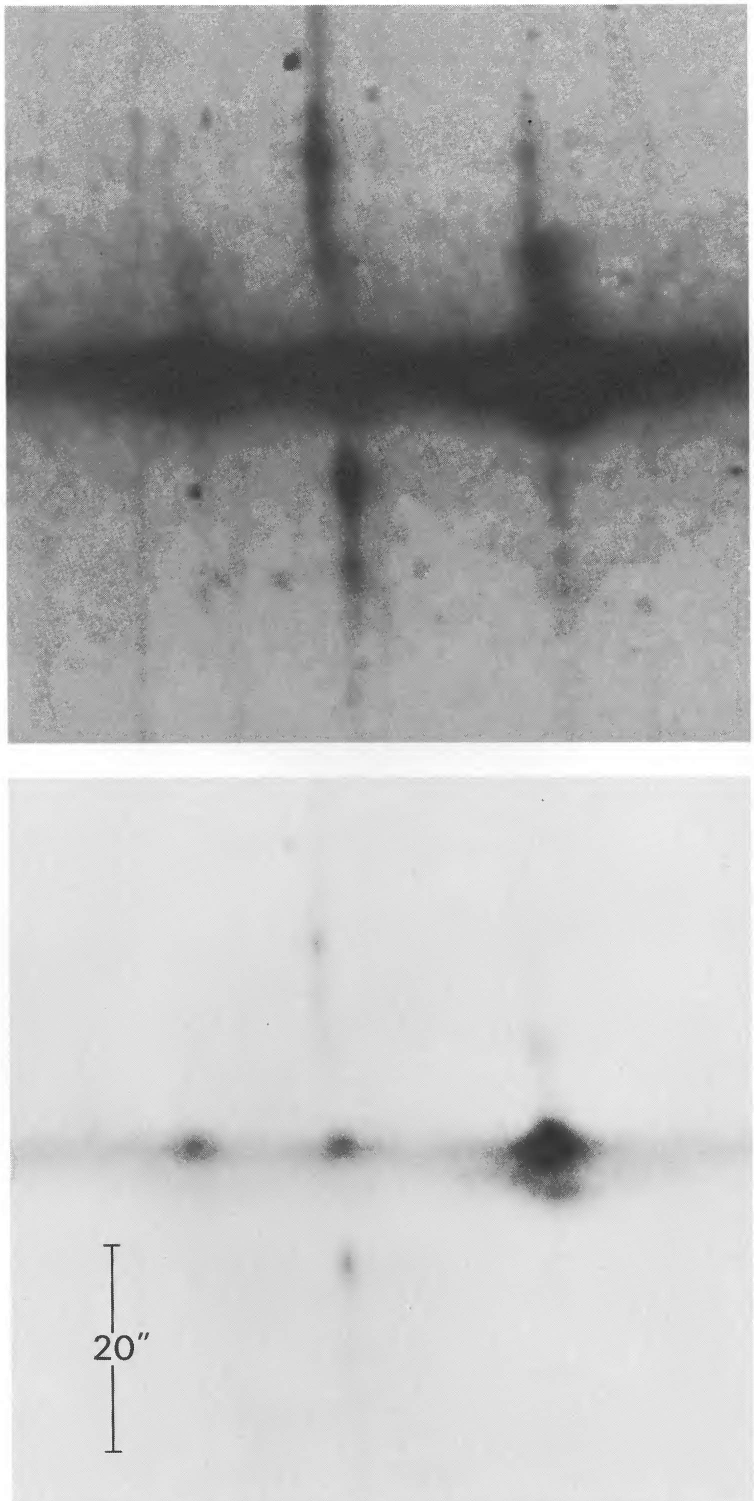

FIG. 8.—KPNO ICCD Hα + [N II] spectra of the center of M51 at P.A. 180°, which crosses the ring's bright northeast limb. North is at the top in this and all subsequent figures. The upper panel is windowed to show low-surface-brightness detail, and the lower panel to show details in the nucleus and cloud. The instrumental profile can be judged from the diffuse disk emission and the knotty H II regions which fall along the slit. Note the discontinuities in the line ratios and line widths at the edges of the ring and the cloud. The unresolved bright spots are cosmic-ray events.

FORD *et al.* (*see* page 137)

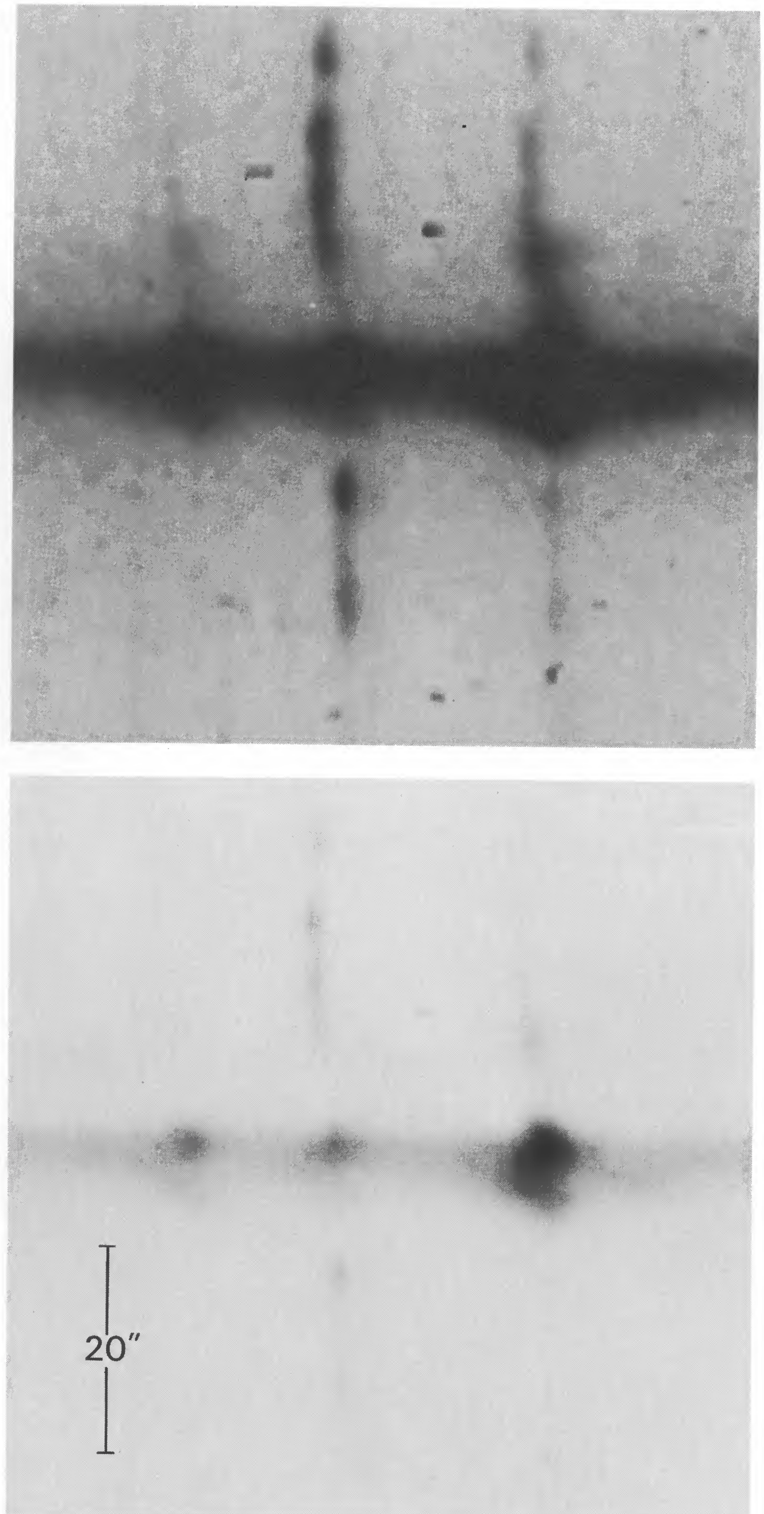

FIG. 9.—Same as Fig. 6, but at P.A. 169°, which crosses the center of the XNC

FORD *et al.* (*see* page 137)

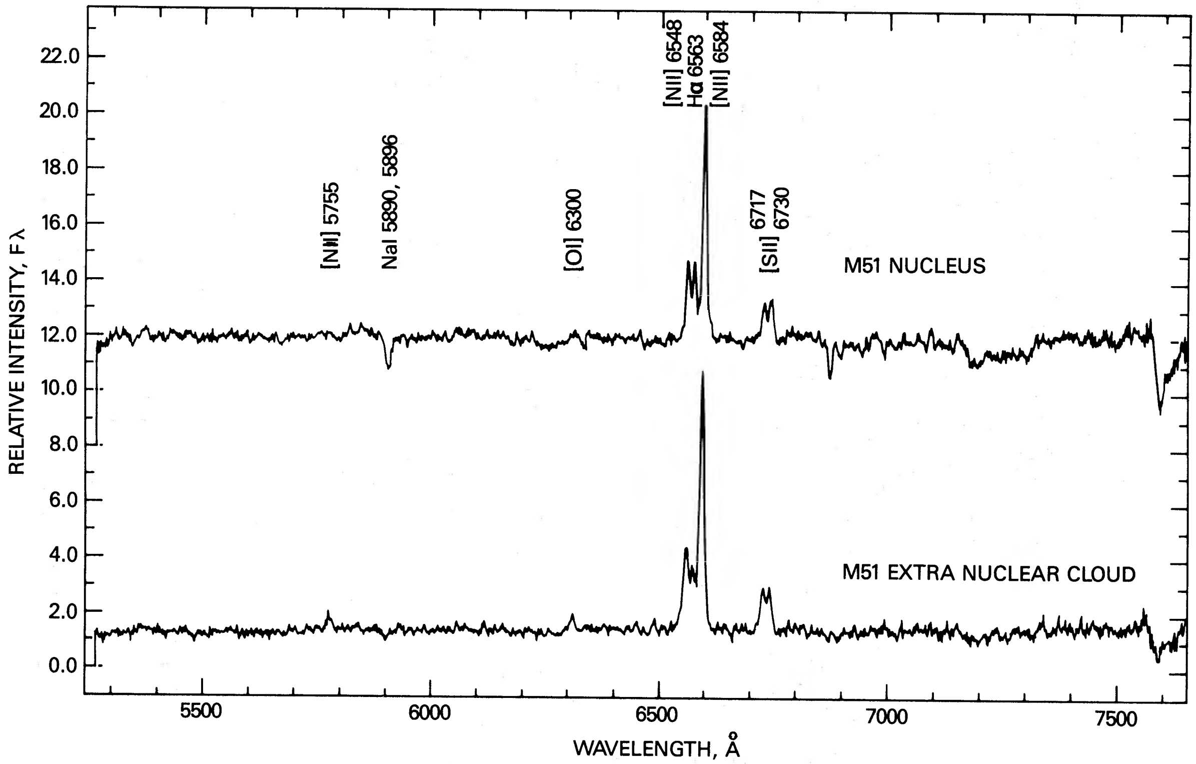

FIG. 7a

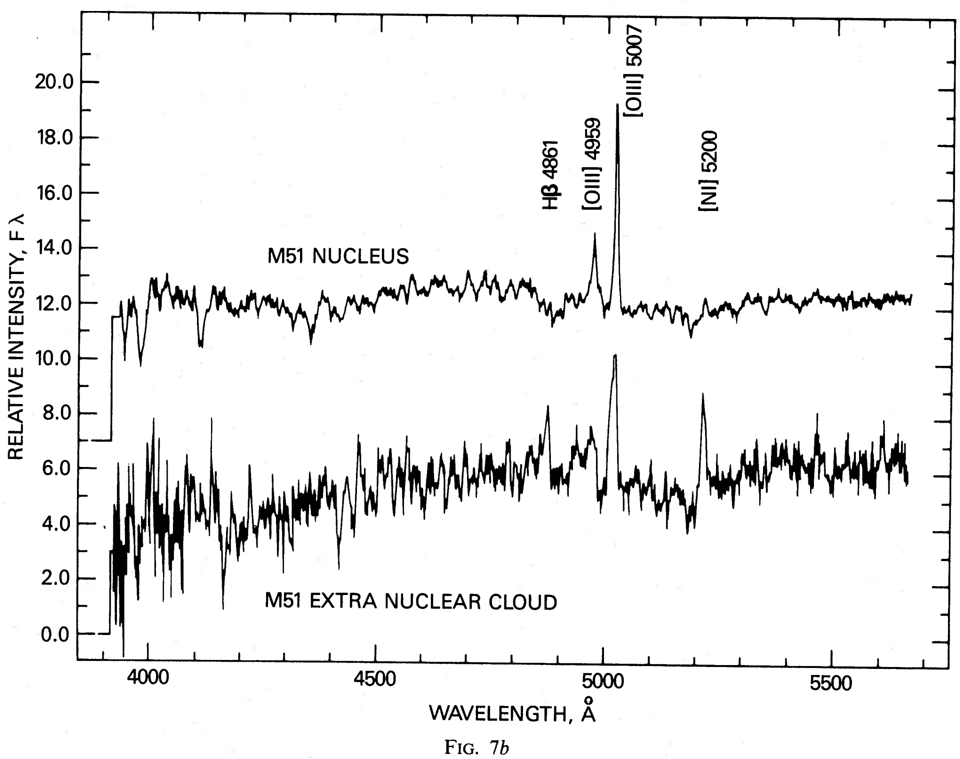

FIG. 7b

FIG. 7.—(a) A pair of sky-subtracted Lick ITS scans of the nucleus and southern cloud in the red spectral region. The Hα + [N II] emission lines are more blended in the cloud than in the nucleus, and [N II] emission is stronger in the cloud than in the nucleus. (b) Lick ITS scans of the nucleus and cloud centered near [O III] λ5007. The cloud has strong emission at [N I] λ5200, which is weak or absent in the nucleus.

their value and used a Whitford reddening law (Miller and Mathews 1972) to calculate the dereddened intensities given in columns (7) and (8). The absolute Hα intensities for each region and instrument are listed in the next-to-last row of Table 4. Comparison of the ITS and SIT calibrations shows that the absolute Hα fluxes differ by a factor of ~3.

The last row in Table 4 provides the electron densities derived from the ratios $I(\lambda6716)/I(\lambda6731)$. The densities were calculated from three-level atom equations (McCall 1984) which incorporate Mendoza's (1983) atomic data. Apart from an apparently erroneous value of $I(\lambda6731)$ in column (4), the [S II] line ratios give consistent densities of a few hundred electrons cm^{-3}.

The Kitt Peak observations were taken with the Ritchey-Chrétien spectrograph and a Texas Instruments 800 × 800 pixel CCD which was coupled to a two-stage RCA image intensifier with a transfer lens set at f/2.0. The spectrophotometric pictures in the red and blue were respectively centered on Hα and [O II] λ3727. The slit was set to 1″.3 × 8′ and used with KPNO grating No. 390 (1200 lines mm^{-1}), giving 2.2 Å resolution (FWHM) at Hα (first order) and 1.2 Å resolution at [O II] λ3727 (second order). Details of the observations are given in Table 3.

Figures 8 and 9 show enlargements of the Hα + [N II] complex at: (1) a 180° position angle, which places the slit across the nucleus, XNC, and bright limb of the ring; and (2) a position angle of 169°, which is along the line that bisects the nucleus, ring, and XNC. The top panel was windowed to show faint emission, whereas the bottom panel shows details in the nucleus and bright XNC center. The top panel shows broad wings on the XNC, and the lower panel shows a striking asymmetry in the XNC profile, with marked attenuation on the red side. This asymmetry was also noticed by RC, although their large aperture (5″) did not enable them to pinpoint the spatial origin of the feature. In the 169° position angle spectrum, the absorption feature isolates a weak emission feature which is centered ~10.7 Å (~500 km s^{-1}) redward of the systematic velocity. The emission from the ring is much narrower than in the XNC but is clearly broader than the instrumental profile, which can be gauged from the Hα emission in the knotty H II regions which fall along the slit. Both figures show an abrupt reversal of the [N II]/Hα ratio and narrowing of the lines at the edge of the XNC and ring; these reversals were also noted by GDVG in their spectra at P.A. 171°.5. The gas in the disk external to the ring and XNC has line widths and line ratios characteristic of H II regions. We conclude that the kinematical and excitation anomalies are confined to and arise from the optical and radio spatially distinct regions shown in Figures 1 through 5.

Figures 10 and 11 (Plates 20 and 21) show enlargements of the [O II] λλ3726/3729 spectra. Figure 10 reproduces two different windowings of the 180° position angle spectrum, and Figure 11 does the same for the 169° position angle setting. A slight redward attenuation of the XNC line profile is suggested by Figure 11, but it is much less distinct than in Figure 9. The [O II] λλ3726/3729 doublet is well resolved in the ring and shows that the gas therein is in the low-density limit. The emission lines in the ring appear to be slightly curved in the 169° position angle spectrum, wherein the slit bisects the ring. At 180°, where the slit crosses the (limb-brightened) edge of the ring, the lines are straight.

We analyzed the 180° spectrophotometric data by slicing the picture parallel to the dispersion. Each slice spanned five rows

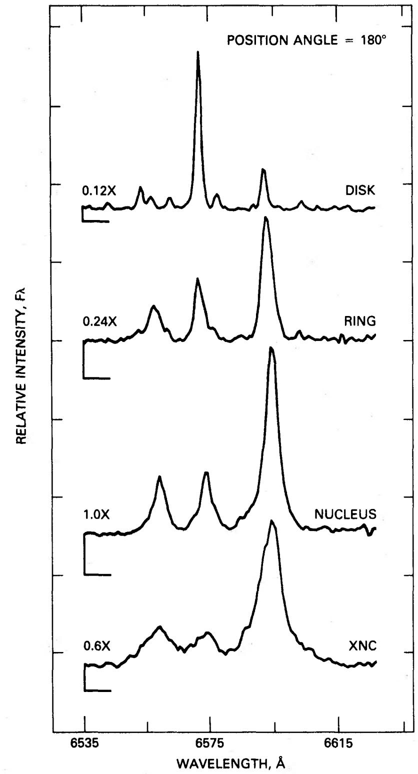

FIG. 12.—Intensity cuts through Fig. 8 parallel to the dispersion. Each spectrum is labeled with the name of the spatial feature. The positions of the cuts relative to the nucleus and their widths are, from top to bottom: 66″ north, 21″ wide; 8″.7 north, 8″.7 wide; 0″.0, 2″.0 wide; and 4″ south, 2″.0 wide.

(3″), which we summed into a single spectrum. The slices were separated by four rows (2″.4). Figure 12 shows slices across the top of the XNC, across the nucleus, and through the center of the ring. The figure also includes a sum across 31 rows (19″) of the relatively weak emission in the disk and H II regions 66″ north of the nucleus. The cuts through the XNC and nucleus again show that there is considerably more line broadening in the XNC than in the nucleus. It is also evident that there is a core and wing structure in the XNC with emission extending ~22 Å (~1000 km s^{-1}) redward of the line center. Comparison of the XNC and nuclear cuts demonstrates that the [N II]/Hα ratio reaches a maximum in the XNC. Because of the relatively strong Hα absorption in the underlying nuclear continuum, the effect would be even more pronounced had we used RC's technique of removing the underlying continuum by subtracting a matching, but emission-line-free, galaxy spectrum.

The slices through the nucleus and ring show that the excitation and core-line widths are similar. The major differences between the two regions are that the nuclear lines have symmetrical wings which extend ±12 Å (±550 km s^{-1}) at zero intensity.

Table 5 lists the heliocentric radial velocities, line ratios, and line profiles which we measured in each of the slices. Column (1) gives the positions of the slices in arc seconds north (+) or south (−) of the nucleus. Column (2) lists the feature which appears at that position. Columns (3) and (4) give the heliocentric radial velocities of the H I λ6562.8 line peak and the weighted average of the [N II] λ6548.1 (weight-$\frac{1}{3}$) and [N II] λ6583.4 (weight-1) peaks. The velocities were derived from a

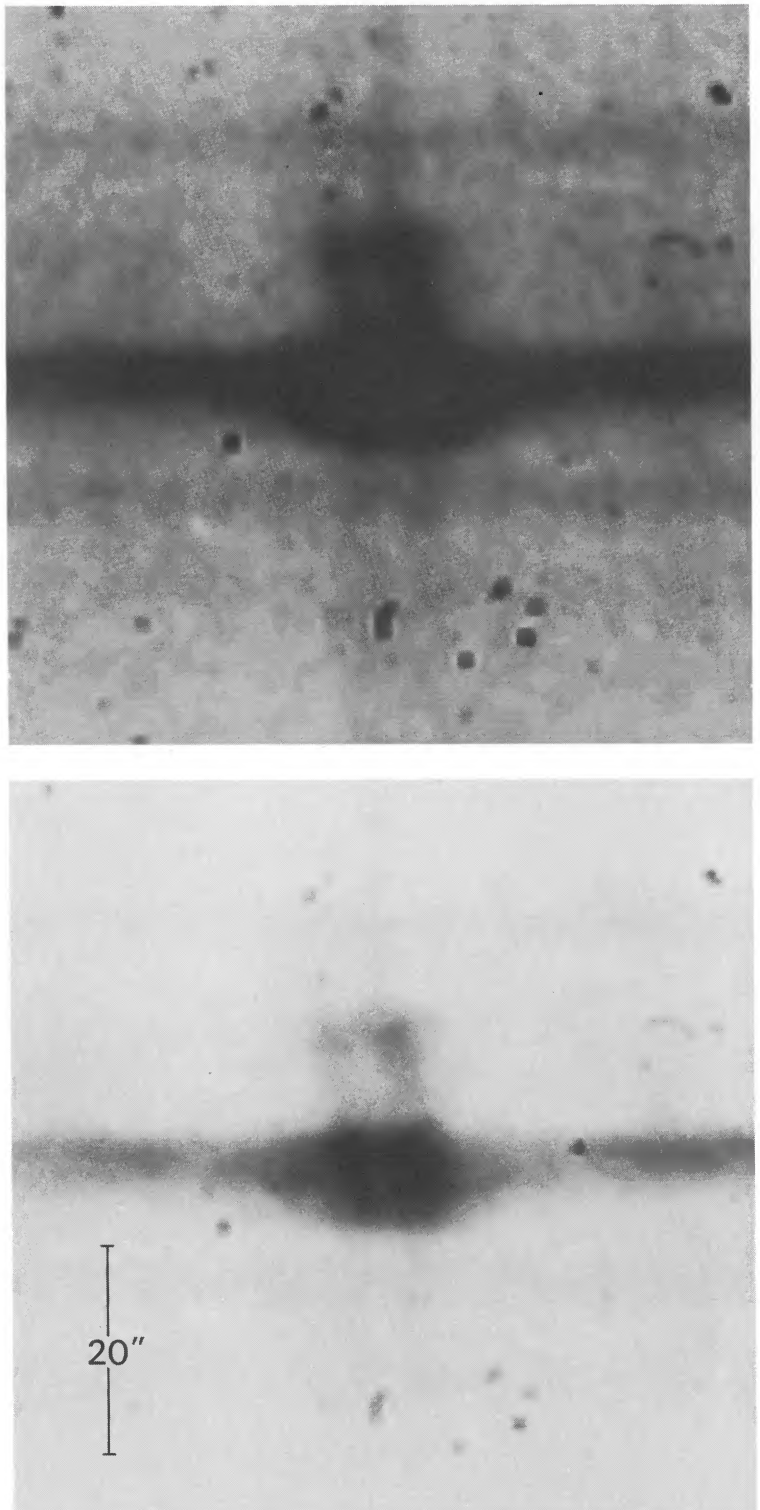

FIG. 10.—KPNO ICCD spectra of the nucleus of M51 centered on the [O II] $\lambda\lambda$3726/3729 doublet at P.A. 180°. The two panels show different windowings of the same data. Note that the gas in the ring is in the low-density limit, and that the doublet ratio must be near unity in the nucleus and XNC. The small dark spots are cosmic-ray events.

FORD *et al.* (*see* page 139)

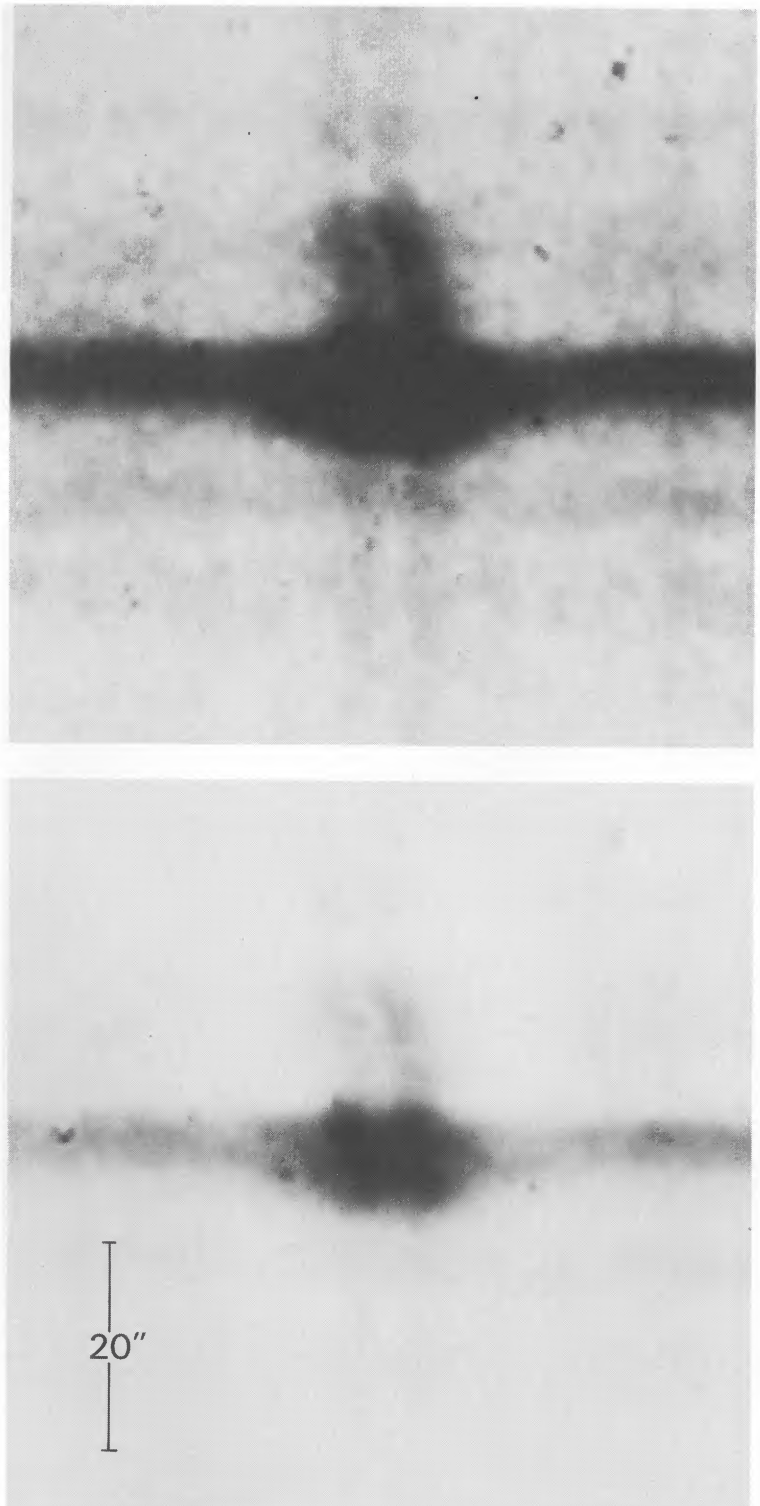

FIG. 11.—Same as Fig. 8, but at P.A. 169°

FORD *et al.* (*see* page 139)

TABLE 5

CHARACTERISTICS OF THE EMISSION LINES IN THE CENTER OF M51

					[N II] λ6584				
POSITION (1)	IDENTIFICATION (2)	$v_{H\alpha}$ (km s^{-1}) (3)	$v_{[N II]}$ (km s^{-1}) (4)	I([N II] λ6584)/I(Hα) (5)	FWHM (km s^{-1}) (6)	FWQM (km s^{-1}) (7)	FWZI (km s^{-1}) (8)	I(λ6717)/I(λ6731) (9)	n_e (cm^{-3}) (10)
+13″2	5″4 disk average	374	379'	0.23	120	220	450	1.36	100
+12.0	Disk	372	381[a]	0.49	110			1.11	390
+9.6	Ring	387	410	1.18	200	360	890	1.14	340
+7.2	Ring	410	435	1.67	180	280	640	(1.18)[b]	(290)
+4.8	Ring	449	455	3.03	210	280	610	(1.03)[b]	(530)
+2.4	Ring-nucleus	478	483	3.95	200	250	880	(1.17)[b]	(300)
+0.0	Nucleus	492	476	3.26	190	310	1100	0.95	720
−2.4	XNC-nucleus	469	471	3.40	310	530	1940	1.05	490
−4.8	XNC	464	497	6.11	370	670	1990	1.08	440
−7.2	XNC	504	509	2.39	210	440	2130	(1.39)[b]	(70)
−9.6	Disk	492	497[a]	0.28	130			1.05	490
−12.0	Disk	503	497[a]	0.18	120	220			
−14.4	Disk	508	503[a]	0.28	120	250			
−16.5	Disk	519	514[a]	0.33	150	270			
−18.6	Disk	525	510[a]	0.41	140	200			
−21.0	Disk	524	532[a]	0.47	160	330			

[a] [N II] λ6584 only.
[b] Because of peculiar line profiles, the ratio is based on the peak heights rather than the areas.

cubic polynomial fit of a neon comparison spectrum taken immediately after the M51 observations. Cuts through the comparison spectrum showed there was no significant distortion over the region of interest; consequently, we derived the dispersion from the comparison spectrum averaged between 29″ north and 22″ south. Our mean heliocentric velocity at the position of the nucleus is 484 km s^{-1}, which is close to the nuclear value of 482 km s^{-1} derived by GDVG.

The ratios of the [N II] λ6584/Hα peak intensities are listed in column (5). We characterized the [N II] λ6584 line profile by measuring the full width at half maximum (FWHM, col. [6]), the full width at quarter maximum (FWQM, col. [7]), and the full width at zero intensity (FWZI, col. [8]). The latter quantity was taken as twice the half width at zero intensity of the red wing of [N II] λ6584. There is good agreement between our FWHM and those measured by GDVG at P.A. 171°5. Finally, column (9) gives the ratios of the I(λ6717)/I(λ6730) integrated intensities, and column (10) gives the implied densities in the S^+ line formation region. Due to the weakness of the [S II] emission in the disk, the ratio was measured only in an averaged disk spectrum.

Figure 13 shows intensity slices through the ring, nucleus, XNC, and disk in the 169° position angle spectrum. The major difference between the spectra at the two position angles is the presence of a conspicuous emission bump on the red wing of the XNC [N II] λ6584 emission line at the position angle which bisects the XNC (169°). This feature, which can be seen in Figure 9, is ~10.3 Å (470 km s^{-1}) redward of the peak velocity in the XNC and reaches maximum intensity 2″ south of the nucleus. However, the conspicuous asymmetry in the core of the line (cf. Fig. 9, lower panel) is so subtle it does not show in single-row slices through the picture.

Figures 14 and 15 show [O II] λλ3726/3729 intensity profiles averaged across the ring, nucleus, and XNC at position angles 180° and 169°. From the symmetry of the profiles in the nucleus and XNC, it is evident that the line ratios are close to 1 at those positions. It is also clear that the line ratio in the ring is in the low-density limit (0.67). Table 6 summarizes our ITS [S II] and ICCD [S II] and [O II] density measurements, using RC's (uncertain) [S II] temperature, 7630 K. The measurements are quite consistent with one another and show that the density in the S^+ and O^+ line-forming regions are ~400 cm^{-3} in the XNC and ~600 cm^{-3} in the nucleus. Because of the

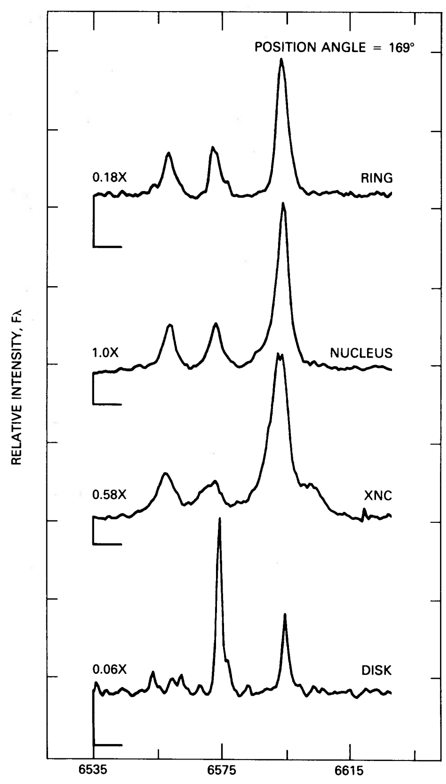

FIG. 13.—Intensity cuts through Fig. 9 parallel to the dispersion. The positions of the cuts relative to the nucleus and their widths are, from top to bottom: 7″4 north, 8″7 wide; 0″0, 2″0 wide; 3″4 south, 2″0 wide; and 23″ south, 27″ wide.

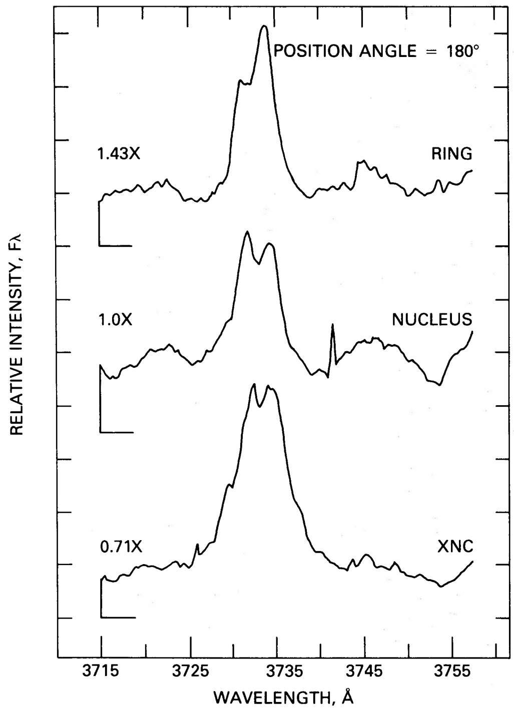

FIG. 14.—Intensity cuts through Fig. 10 parallel to the dispersion. The positions and widths of the cuts are: 8″.7 north, 8″.7 wide; 0″.0, 2″ wide; and 4″ south, 2″ wide. Note that the gas in the ring is in the low-density limit and that the doublet ratios in the nucleus and XNC are near unity.

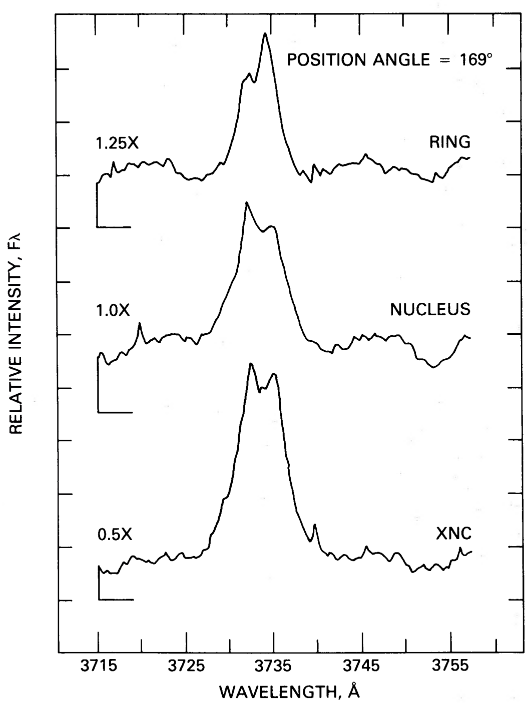

FIG. 15.—Intensity cuts through Fig. 11 parallel to the dispersion. The positions and widths of the cuts are: 8″.7 north, 8″.7 wide; 0″.0, 2″ wide; and 4″ south, 2″ wide. There is no evidence of the high-velocity cloud seen in Figs. 7 and 11. The sharp feature at the peak of λ3726.05 may be due to a cosmic-ray event.

TABLE 6

[S II] AND [O II] ELECTRON DENSITIES IN M51

Position	ITS [S II] (cm^{-3})	ICCD [S II] (cm^{-3})	ICCD [O II] (cm^{-3})
Ring	...	(340)	≤100
Nucleus	640	720	480
XNC	370	440	480

peculiar [S II] line profiles across the ring, the [S II] density must be disregarded. The [O II] line profiles show that the density is very low in the ring.

III. DISCUSSION

a) *Ionization*

Identifying the ionization mechanisms in the XNC and ring should be one of the keys to understanding their origins. RS argued that the gas throughout the center of M51 is photoionized by a power-law continuum from a central nonstellar source. Their strongest arguments for photoionization were the isotropic radial gradients in emission-line intensity ratios, and the absence of the strong correlation between observed line-intensity ratios and line widths that would be expected in shock-ionized gas. RC strengthened the case for photoionization by using the nuclear line ratio $I(\lambda4959 + \lambda5007)/I(\lambda4363)$ ($r \leq 2''.5$) to derive an upper limit to the temperature in the nucleus, $T \leq 14{,}900$ K, which precludes the high-temperature zone in a shock front which will excite [O III] λ5007. In spite of these plausible arguments, we believe that our new observations pose considerable difficulties for the conclusion that the entire central region is photoionized. The first problem is that of a radio and optically bright ring and cloud paired across the nucleus. There is no natural explanation for the radio emission and unusual morphology in a photoionization model. A second difficulty is that RS based their conclusions on an assumed smooth, radial change in line ratios, and lack of correlation between line widths and line ratios. However, with the improved spatial resolution of our spectroscopic pictures and monochromatic optical and radio images, it is clear that the line widths and line ratios have abrupt discontinuities at the edges of the ring and XNC. These discontinuities were also noted by GDVG in their spectra at 171°.4 position angle, wherein the slit bisects the ring and XNC.

In our view, the aggregate of ring and XNC characteristics have a natural explanation in gas which is heated and excited by shocks. The line ratios are similar to those found in supernova remnants (SNRs) in precisely the locations where the radio data shown compression of the ambient magnetic field and where the line widths show that there are mass motions capable of driving shocks. The conclusion that the presence of a radio-emitting relativistic plasma is indicative of optical shocks is supported by the rough equality of the pressure in the relativistic gas ($P_{XNC} \approx 4.4 \times 10^{-9}$ dynes cm^{-2}, derived in the next section) and the gas pressure in the [S II] emitting region, $nkT \approx 8.5 \times 10^{-10}$ dynes cm^{-2}, where we have used the average [S II] density, $n_e \approx 400$ cm^{-3}, and the [S II] line weighted temperature derived from the model shock, $T \approx 15{,}000$ K. Fosbury *et al.* (1978) inferred a similar equality in NGC 1052, where they measured an [O III] λλ4363/5007 temperature $T \approx 39{,}000$ K. Because of the high temperature they concluded, as did Koski and Osterbrock (1976), that the gas is shock heated (but see also Keel and Miller 1983; Rose and Tripicco 1984).

Table 7 compares the reddening-corrected line intensities in the XNC, M51's nucleus, a filament in the SNR Pup A (Dopita, Mathewson, and Ford 1977), and the radio galaxy Cyg A (Osterbrock and Miller 1975). The latter has a strong optical nonthermal continuum and is probably largely photoionized by the ultraviolet extension of that continuum. The most notable differences between the XNC and nucleus are that [O II] λ3727, [N I] λ5200, and [O I] λ6300 are much stronger relative to [O III] λ5007 in the XNC than in the nucleus. Qualitatively, the XNC line ratios are similar to Pup A, whereas the nucleus is closer to Cyg A. The similarity of the XNC and Pup A lends plausibility to our conclusion that the gas in the XNC (and ring) is shock excited. Pup A shows that nature can use shocks to produce spectra similar to that of the XNC. However, comparison with Cyg A illustrates the fact that power-law photoionization can also produce spectra with a wide range of ionization stages, and which resemble shock spectra. Even though we cannot make a definitive choice between the two kinds of ionization until an [O III] temperature is measured in the XNC, we believe that the evidence greatly favors shock ionization and excitation in the XNC and ring.

We investigated the XNC chemical composition by using a recently developed Stromlo modeling code for radiative shocks, MAPPINGS, which was generously made available to us by Mike Dopita. The new code (Binette, Dopita, and Tuohy 1984) incorporates pre-ionization ahead of the shock, transfer of UV photons generated in the hot plasma through the downstream recombination zone, charge-transfer reactions, Auger ionization and heating, a large number of coolants, and (as we used the code), Mendoza's (1983) atomic coefficients. However, because of the ~20 hr required to run the code on the Stromlo Observatory VAX 780 with inclusion of radiative transfer, we ran most models with a simplified code which excludes photoionization by the photons produced in the shock front. The line ratios from a shocked gas are primarily sensitive to chemical abundances rather than to the initial conditions of the shock (Dopita 1981). Consequently, we were able to reproduce the XNC line ratios with a wide range of initial conditions (pre-shock density, magnetic field, ionization, and shock velocity), but with only a narrow range of abundances for N, O, and S. The initial conditions and abundances for one of our models which gives a good match to the XNC are listed in Table 8. The shock velocity of 141 km s^{-1} was chosen because it is comparable to the observed half width at half maximum in the XNC line profile; however, higher or lower velocities also give good fits. We estimate that the uncertainties in the N, O, and S abundances introduced by initial conditions and modeling procedure are ~25%.

TABLE 7

COMPARISON OF LINE INTENSITIES WITH SHOCK-IONIZED AND PHOTOIONIZED GAS

Emission Line	XNC	Nucleus	Shock Model	Pup A	Cyg A
[O II] λ3727	3.63	2.46	1.76	...	1.62
H I λ4861	0.38	...	0.32	0.34	0.32
[O III] λ4959	0.51	0.86	0.24	0.09	1.26
[O III] λ5007	0.84	2.31	0.70	0.25	3.99
[N I] λ5200	0.44	≤0.14	0.48	0.13	0.10
[N II] λ5755	0.32	...	0.20	...	0.03
[O I] λ6300	0.44	...	0.02	0.23	0.36
[N II] λ6548	1.50	1.17	1.50	1.41	0.62
H I λ6563	1.00	1.00	1.00	1.00	1.00
[N II] λ6584	4.65	3.78	4.42	4.14	2.00
[S II] λ6717	0.71	0.54	0.76	0.45	0.54
[S II] λ6731	0.63	0.55	0.73	0.55	0.49

TABLE 8

A. PHYSICAL CONDITIONS OF XNC SHOCK MODEL

Shock Conditions	
Shock velocity	141 km s^{-1}
Post-shock temperature	300,000 K
$I_{H\beta}$	2.56 × 10^{-5} ergs cm^{-2} s^{-1} sr^{-1}
$I_{forbidden}$	9.87 × 10^{-4} ergs cm^{-2} s^{-1} sr^{-1}
I_{total}	1.05 × 10^{-2} ergs cm^{-2} s^{-1} sr^{-1}
Pre-shock Conditions	
Density	3 cm^{-3}
Temperature	8200 K
Magnetic field	0 G
Fractional ionization	Shull and McKee 1979, Model G

B. ELEMENTAL ABUNDANCES BY NUMBER RELATIVE TO HYDROGEN

Element	XNC Shock Model	Orion[a]
He	1.0 × 10^{-1}	1.0 × 10^{-1}
C	4.0 × 10^{-5}	3.2 × 10^{-2}
N	1.76 × 10^{-3}	5.7 × 10^{-5}
O	8.0 × 10^{-4}	5.6 × 10^{-4}
Ne	2.0 × 10^{-4}	...
Mg	2.0 × 10^{-5}	...
Si	4.0 × 10^{-6}	...
S	5.3 × 10^{-5}	2.6 × 10^{-5}
Cl	5.0 × 10^{-7}	...
Ar	5.0 × 10^{-6}	...

[a] Peimbert, Torres-Peimbert, and Rayo 1978; value for carbon from Torres-Peimbert, Peimbert, and Daltabuit 1980.

The line intensities from the model are listed in Table 7 along with the reddening-corrected intensities of the XNC and nucleus. Except for [O I] λ6300, the match to the XNC spectrum is quite good. We were unable to find a set of initial conditions and abundances that would simultaneously give a strong [O I] λ6300 and a good match to the [O II], [O III], [N II], and [S II] emission lines. Since M51 has a central X-ray source that might weakly ionize and heat a large region that could give rise to [O I] emission, we ran several models which included a power-law ($\alpha = -0.7$) X-ray source at the shock front and different ionization parameters $U_x = N_x c^{-1} n^{-1}$, where $N_x c^{-1}$ is the density of downstream hydrogen ionizing photons and n is the density in the recombination zone. Ionization parameters between 2 × 10^{-6} and 2 × 10^{-5} gave I([O I] λ6300)/I(Hβ) ratios between 0.30 and 1.59, and I([N I] λ5200)/I(Hβ) ratios between 1.69 and 10.89, and poor overall fits to the other lines. The strengths of [O I] and [N I] show that suitable linear combinations of radiative shock models and models which simulate inclusion of an external X-ray source probably would produce a good match to the observed XNC spectrum. Because this procedure is arbitrary without information about the distribution of X-ray emitting plasma and shocked gas, we did not attempt it. Nonetheless, we conclude that X-ray heating probably is important in accounting for the strong [O I] λ6300 and [N I] λ5200 emission.

Halpern and Steiner (1983) have suggested that X-ray ionization may account for the class of low-luminosity, low-ionization active galaxies ("Liners") defined by Heckman

(1980). Although the XNC has line ratios like a "Liner," we think that X-rays must play a minor rather than major role in its photoionization. First, there are the previously stated problems of explaining the morphology, line widths, and radio emission with photoionization. Second, and more fundamental, there is a problem with ionization equilibrium. The total flux of ionizing photons between the Lyman limit and 10 KeV, with an $\alpha = -0.7$ power law normalized to 10^{40} ergs s^{-1} (one-third of the total flux), is 4.3×10^{49} photons s^{-1}, whereas the observed number of recombinations is $R_{\rm XNC} \approx L_{{\rm H}\beta,\,{\rm XNC}} \times \alpha_B \times \alpha_{{\rm H}\beta}^{-1} \times (h\nu_{{\rm H}\beta})^{-1} \approx 2 \times 10^{51}$ s^{-1}, where α_B and $\alpha_{{\rm H}\beta}$ are effective recombination coefficients, and $L_{{\rm H}\beta,\,{\rm XNC}} \approx 8.7 \times 10^{38}$ ergs s^{-1} (cf. Table 9). The observed X-ray luminosity is insufficient to support the observed recombination rate.

The most certain conclusion from comparison of the models with the XNC is that N/H and N/O are extraordinarily high. Table 8 includes N, O, and S abundances in the Orion nebula (Peimbert, Torres-Peimbert, and Rayo 1978), which presumably is representative of abundances in the local interstellar medium. The N/H and N/O ratios are ~ 20 times higher than near the Sun, and higher than any previously observed extragalactic abundances. These abundance ratios show that the N/H and N/O gradients in late-type spirals found by Searle (1971) and confirmed by Shields (1974) and Smith (1975) continue, and perhaps steepen, into the centers of late-type galaxies.

An enhanced N/O ratio is predicted in CNO-processed material (e.g., Arnett 1971) and found in some nebulae around highly evolved stars which are thought to have (or have had) high masses. Examples of these are Type I planetary nebulae (Peimbert and Torres-Peimbert 1983), nebulae such as NGC 6888 around the WN6 star HD 192163 (Parker 1978), and the Pup A SNR (Dopita, Mathewson, and Ford 1977). In view of this, we suggest that there is a progressive change in the mass function toward the center of late-type spirals which favors massive stars. Alternatively, or perhaps in conjunction with the gradient, galaxies such as M51 may go through nuclear episodes of extreme WN star production such as those observed by Osterbrock and Cohen (1982) and Kunth and Sargent (1981).

Baldwin, Phillips, and Terlevich (1981) have developed a galaxy classification scheme based on emission-line ratios which provides another way to assess excitation mechanisms. They show that plots of selected, combined emission-line ratios versus $I(\lambda3727)/I(\lambda5007)$ cleanly separate H II regions, galaxy nuclei which are thought to be photoionized, and galaxy nuclei which are thought to be shock-excited. The XNC plots among the latter in all of their diagrams.

In our view, the arguments of RS and RC for photoionization are likely correct in the nucleus. However, based on the preceding considerations, we conclude that the ring and XNC are excited by shocks.

b) Physical Characteristics of the Nuclear Emission Regions

Table 9 lists the derived physical characteristics of M51's nuclear emission regions. The sizes of the nucleus and XNC were derived by fitting Gaussians to the radio maps and assuming a distance of 9.6 Mpc (Sandage and Tammann 1974). The sizes of the ring are its largest and smallest dimensions. The first step in deriving the XNC Hβ luminosity was to average the observed $2'' \times 2''$ ITS Hα flux, 3.0×10^{-14} ergs cm^{-2} s^{-1}, and the $2'' \times 2''$ Hα flux derived from video camera pictures, 2.27×10^{-14} ergs cm^{-2} s^{-1}, to obtain the average value 2.6×10^{-14} ergs cm^{-2} s^{-1}. We corrected this for interstellar reddening and multiplied by the reddening-corrected ITS Hβ/Hα ratio, to obtain $F_{{\rm H}\beta}$ $(2'' \times 2'') = 2.0 \times 10^{-14}$ ergs cm^{-2} s^{-1}. Our radio and optical pictures show that the optical emission is at least approximately proportional to the radio emission. Consequently, we estimated the ratio of the total Hβ flux to the $2'' \times 2''$ flux by measuring the ratio of the total XNC 6 cm flux to the flux in a $2'' \times 2''$ area in the center of the cloud, obtaining a value of 4. Correction for the distance then gives a luminosity $L_{{\rm H}\beta,\,{\rm XNC}} = 8.7 \times 10^{38}$ ergs s^{-1}. The ratio of the total 6 cm nuclear flux ($2''.2 \times 3''.5$) to the flux in a $2'' \times 2''$ area centered on the nucleus is ~ 1.23. We estimated the total nuclear Hβ flux by multiplying this geometrical correction factor and an assumed $I({\rm H}\beta)/I({\rm H}\alpha)$ ratio (0.38) times the dereddened nuclear Hα flux in Table 4 to obtain $F_{{\rm H}\beta,\,{\rm nucleus}} = 2.6 \times 10^{-14}$ ergs cm^{-2} s^{-1}, which gives a luminosity $L_{{\rm H}\beta,\,{\rm nucleus}} = 2.8 \times 10^{38}$ ergs s^{-1}. As a check on our procedure, we used the same technique to estimate the observed Hα + [N II] flux inside a $3''.5$ aperture, obtaining 7.5×10^{-13} ergs cm^{-2} s^{-1}. This value is in satisfactory agreement with Peimbert's

TABLE 9

PHYSICAL CHARACTERISTICS OF M51'S NUCLEAR EMISSION REGIONS

Characteristics	Ring	Nucleus	XNC
Distance (pc)	415	0	165
Position angle	$-15°$	0°	166°
Major axis (pc)	540	50	135
Minor axis (pc)	405	25	100
Volume (cm^3)	1.6×10^{63}	6.8×10^{59}	2.4×10^{61}
$L_{{\rm H}\beta}$ (ergs s^{-1})	(1.6×10^{39})	2.8×10^{38}	8.7×10^{38}
Filling factor, ϵ	(9.9×10^{-5})	9.3×10^{-3}	1.8×10^{-3}
Mass ($M_\odot$)	(1.9×10^4)	4.4×10^3	2.1×10^4
Kinematical age, t_k (yr)	1.4×10^6	6.3×10^4	1.1×10^5
$L_{\rm optical}$ (ergs s^{-1})	(6.6×10^{41})	1.2×10^{41}	3.6×10^{41}
$E_{\rm total}$ (ergs s^{-1})	(2.7×10^{55})	2.4×10^{53}	1.2×10^{54}
$L_{\rm X\text{-}ray}$ (ergs s^{-1})	...	3.0×10^{40}	...
P (1465 MHz) (W Hz^{-1})	2.88×10^{20}	3.98×10^{19}	1.62×10^{20}
P (4885 MHz) (W Hz^{-1})	1.10×10^{20}	1.82×10^{19}	5.13×10^{19}
L (ergs s^{-1})	4.2×10^{37}	7.1×10^{36}	2.3×10^{37}
$U_{\rm min}$ (ergs)	5.8×10^{53}	6.0×10^{51}	9.8×10^{52}
$B(U_{\rm min})$ (μG)	63	305	208
τ (GeV) (yr)	2.1×10^5	9.0×10^3	1.9×10^4
$P(U_{\rm min})$ (dynes cm^{-2})	4.0×10^{-10}	9.6×10^{-9}	4.4×10^{-9}

(1968) and Turnrose's (1976) observed Hα + [N II] fluxes ($r = 3''.5$), which are 6.4×10^{-13} ergs cm^{-2} s^{-1} and $\gtrsim 7.7 \times 10^{-13}$ ergs cm^{-2} s^{-1}.

We calculated the fractions of the volumes filled with emitting gas, ϵ, from the equation

$$\epsilon = \frac{L_{\mathrm{H}\beta}}{\alpha_{\mathrm{H}\beta} n_e^2 V h\nu_{\mathrm{H}\beta}} ,$$

where $\alpha_{\mathrm{H}\beta}$ is the effective Hβ recombination coefficient ($\sim 3 \times 10^{-14}$ s^{-1}) and n_e is the average electron density derived from the [O II] and [S II] doublets. The respective values of ϵ for the XNC and nucleus are 1.8×10^{-3} and 9.3×10^{-3}, which show that the gas is very clumpy or filamentary. We calculated the masses of ionized gas by using the equation

$$M = 1.4 n_e M_{\mathrm{H}} \epsilon V ,$$

which assumes there is a normal helium abundance and that the gas is completely ionized. The results are $M_{\mathrm{XNC}} = 2.1 \times 10^4 M_\odot$ and $M_{\mathrm{nucleus}} = 4.4 \times 10^3 M_\odot$.

Because the ring is heavily blended with the disk in our photographs, we were unable to measure its emission-line flux. Consequently, we estimated its Hβ luminosity and mass by assuming that it has the same average $L_{\mathrm{H}\beta}/L_6$ cm and M/L_6 cm ratios as the nucleus and XNC, which agreed well with one another. These somewhat uncertain estimates are enclosed in parentheses in Table 9.

We estimated kinematical ages for the nuclear emission regions by dividing their transverse sizes [$\surd$(ab)] by the half-width velocity at zero intensity (HWZI). Because the actual expansion velocities are probably considerably lower than the HWZIs, these kinematical ages should be lower limits to the true ages. The ages, which are given in Table 9, suggest that the current activity in the nucleus and XNC are about equally old, whereas the ring is almost an order of magnitude older. Using the velocity half width at half maximum v(HWHM) increases the estimated ages, but preserves the relative sense of the ages.

We used the shock-front model which best matched the XNC spectrum to compute the ratio of the total emission-line luminosity to the Hβ luminosity. Multiplication of this ratio (414) times $L_{\mathrm{H}\beta}$ gives 1.2×10^{41}ergs s^{-1} and 3.6×10^{41} ergs s^{-1} for the total nuclear and XNC optical luminosities. We can now get a rough estimate of the energy released during the lifetimes of the sources by taking the product of the kinematical ages and the total luminosities, obtained 2.4×10^{53} ergs and 1.2×10^{54} ergs.

The 0.1–4 KeV X-ray luminosity in Table 9 was derived from an *Einstein* observatory IPCS picture of M51 (Sarazin 1983) and is the integrated flux from the central region. The low-resolution IPCS picture barely resolves the central complex and shows that it is slightly elongated in the direction of the ring and cloud.

The last entries in Table 9 characterize the radio emission from the ring, nucleus, and XNC. The integrated radio luminosities were derived by extrapolating from the 6 cm and 20 cm luminosities to 10^7 Hz and 10^{11} Hz. The minimum energies and corresponding magnetic fields were derived from the usual precepts (e.g., Moffet 1975) and the assumptions that the total particle energy is 100 times that of the relativistic electrons and that the radio filling factor is 1. The next-to-last row in Table 9 give the time required for a 10 GeV electron to lose one-half its energy, and the last row gives the pressure in the relativistic plasma. The electron half times are an order of magnitude smaller than the kinematical ages of the features, which shows that there must be relativistic electron production within the sources.

c) Origins of the Nuclear Sources

Several authors (Condon *et al.* 1982; van der Hulst, Crane, and Keel 1981) have suggested that the central radio sources in late-type galaxies may be powered by supernovae. Because the XNC and ring appear to be shock excited and have morphologies like many SNRs, it is interesting to compare them to SNRs. Table 10 includes data for Cas A, one of the youngest and most radio-luminous galactic SNRs, and BA 55 (Blair, Kirshner, and Chevalier 1981), an optically bright SNR in M31 which has a spectrum similar to the XNC. It is clear from Table 10 that with respect to size, optical luminosity, and radio luminosity, the nuclear sources in M51 are equivalent to several hundred SNRs. Their inferred total energies ($\sim 10^{54}$ ergs) and kinematical ages ($\sim 10^5$ yr) are two orders of magnitude larger than for luminous galactic SNRs. Put another way, at the distance of M51, Cas A would have an angular diameter of $0''.1$ and a 6 cm flux density 50 times smaller than the XNC. The high degree of 6 cm polarization ($\sim 25\%$ maximum) in the northern source is a strong indication that it is not the superposition of several hudred SNRs. WU have shown that such a superposition would yield very low polarizations. Although we cannot conclusively rule out the possibility that two sites for several hundred supernovae have neatly paired across the nucleus, we think a more unifying explanation can be found by looking for their origin in nuclear events. With this aim, we

TABLE 10

COMPARISON OF M51'S NUCLEAR EMISSION WITH SNRs AND ACTIVE NUCLEI

Object	Size (pc)	$L_{\mathrm{H}\beta}$ (ergs s^{-1})	$L_{6\,\mathrm{cm}}$ (W Hz^{-1})	Reference
Ring	540 × 405	(1.6×10^{39})	1.1×10^{20}	...
Nucleus	50 × 25	2.8×10^{38}	1.8×10^{19}	...
XNC	135 × 100	8.7×10^{38}	5.1×10^{19}	...
Cas A	4	...	8.0×10^{17}	1
BA 55	20	1.6×10^{35}	...	2
Galactic center	~60	...	1.3×10^{19}	3
NGC 1068 nucleus	17 × 39	4×10^{40}	9.2×10^{21}	4
NGC 1068 linear source	700		1.7×10^{22}	4, 5

REFERENCES.—(1) Weiler *et al.* 1983. (2) Blair, Kirshner, and Chevalier 1981. (3) Ekers 1980; van der Hulst 1980. (4) Wilson and Ulvestad 1982, 1983. (5) Neugebauer *et al.* 1980.

include in Table 10 a comparison with the galactic center and the Seyfert galaxy NGC 1068. M51's nuclear activity is intermediate between the two, being larger and more luminous than the galactic center, and comparable in size to NGC 1068, but less luminous.

As a starting point, we assume that the strong alignment of the XNC and ring across the nucleus and along the direction of nuclear elongation show that (1) the two sources are related and (2) they are powered by events in the nucleus. Two different points of view can then be used to explain the origin of the sources. The first is that the sources are created and powered by jets emanating from the nucleus and interacting with the surrounding interstellar medium. The second is that the sources are discrete plasmoids which were ejected from the nucleus and are now interacting with the disk. We will discuss each of these in turn.

i) *Jets*

On a large scale there is a great deal of evidence that classical radio triples (e.g., Moffet 1975) are powered by beams or jets, which, in some cases, are directly observable (Miley 1980). Strong support is also given to this idea by the examples of complex radio structure which can be explained by precessing beams (Gower *et al.* 1982). Recent papers by Wilson and Willis (1980); Ulvestad, Wilson, and Sramek (1981); WU; and Wilson and Ulvestad (1983) have shown that many Seyfert galaxies have small-scale ($r \approx 1$ kpc), low-luminosity ($L_{\rm radio} \approx 10^{41}$ ergs s^{-1}), linear radio sources which appear to be examples of low-energy beams or jets interacting with the interstellar medium in the parent galaxies. NGC 1068, a well-observed and relatively close ($d = 11.3$ Mpc if $H_0 = 100$ km s^{-1} Mpc^{-1}) example of an active (Seyfert) spiral which shows strong evidence for nuclear jets or beams (WU, Wilson and Ulvestad 1983), is included in Table 10 for comparison. The major differences between M51 and NGC 1068 are that the latter is ~ 100 times more luminous at optical and radio wavelengths than M51 and has radio lobes (the 13″ linear structure) which show a pronounced "leading" S-distortion. WU have shown that the leading S-distortion can be explained by a stationary double beam or jet which is increasingly swept forward at larger radii by the ram pressure from gas in NGC 1068's rotating disk.

RS and RC have already suggested that M51 is a mini-Seyfert. Its radio and optical morphology and luminosity, when compared to the equivalent structures in Seyferts, strengthen this characterization.

Another instructive comparison is with SS 433, a galactic radio, optical, and X-ray source with precessing relativistic jets (Margon *et al.* 1979; Abell and Margon 1979) which is embedded in the nonthermal radio source W50 (Milne 1979; Geldzahler, Pauls, and Salter 1980). Zealy, Dopita, and Malin (1980, hereafter ZDM) and van den Bergh (1979) found two areas of ionized gas paired across SS 433 and inside the radio source. The red spectral regions show strong [O I], [N II], and [S II] with line ratios relative to Hα similar to those in the XNC. ZDM conclude that the filaments are excited by low-velocity shocks (40–60 km s^{-1}) which are powered by the interaction of SS 433's jets with clumps of gas which were previously compressed by the expanding SNR.

There is considerable evidence that the XNC and ring are phenomena in the disk of M51. Although the evidence for noncircular motions north and south of the nucleus is well established (GDVG), it is also true that there is approximate velocity continuity from the velocity of the diffuse disk gas through the ring (cf. Figs. 8 and 9) and into the nucleus, showing that the ionized gas in the ring and XNC largely move with the solid-body rotation of the inner disk. A second argument that the XNC is embedded in the disk is based on its mass and volume. The rms electron density in the XNC is 6 cm^{-3}, which is comparable to the density expected in the disk.[4] Put another way, if a jet is entraining, exciting, and inflating gas in the disk, the mass within the XNC is approximately the amount that would be expected from this volume of the disk. Finally, as noted previously, the ring is limb-brightened on its northeast edge, where it appears to be interacting with a spiral arm which is almost certainly in the disk.

Three facts suggest that there is a jet in M51. First, the nucleus is elongated in both optical and radio emission (at position angle 163°). Second, the optical and radio emission in the disk are aligned across the nucleus in the direction of elongation. Finally, the bow-shaped limb brightening on the south side of the XNC and the change in spectral index from -0.7 at the bright edge to -1.4 on the north edge suggests this is a working surface with steepening of spectral index as the plasma backwashes away from the working surface. It follows that there may be a dual jet emanating from the nucleus of M51 which interacts with the disk of M51 and, through entrainment and compression of the gas in the disk, creates shocks which give rise to the emission, and, by heating the gas, inflate bubbles in the disk. The line broadening in the ring and XNC are then due to turbulent motions of the entrained gas and expansion of the bubbles. The intriguing 500 km s^{-1} redshifted emission in the [N II] λ6584 line may show that the bubble has blown through the far side of the disk and that ionized clouds are being accelerated away from the disk by the presumed hot gas ($T \approx 3 \times 10^6$ K) in the interior of the bubble. The apparent absorption asymmetry in the core of [N II] λ6584 and the absence of the 500 km s^{-1} feature in the [O II] λ3727 line have a natural explanation if there is a patchy distribution of dust inside the bubble. The large size of the northern bubble and its smaller line broadening imply that it is dynamically older than the XNC. Because its transverse size is much larger than the likely disk scale height, it most likely is a bubble that has broken through the disk and burst at the top and bottom. In our view, the southern bubble will eventually evolve into a structure similar to the northern source.

We can use energy and pressure considerations to establish the approximate characteristics of a jet which can power the XNC. The required mechanical energy in the jet, denoted E_j, can be estimated in two ways. The first is to take the minimum energy of the southern radio plasma, 9.8×10^{52} ergs, divided by its characteristic age, 1.1×10^5 yr, giving $E_j \gtrsim 3 \times 10^{40}$ ergs s^{-1}. The second method is to require $E_j \gtrsim L_{\rm radio} + L_{\rm optical} + L_{\rm X\text{-}ray}$. The optical luminosity, $L_{\rm optical} \approx 3.6 \times 10^{41}$ ergs s^{-1}, is the dominant cooling mechanism. The two estimates are in rough agreement, and with reasonable confidence we assume $E_j \gtrsim 10^{41}$ ergs s^{-1}. The jet's mechanical energy is given by

$$E_j = \tfrac{1}{2}\dot{M}_j V_j^2 = \tfrac{1}{2}(\rho_j \pi R_j^2 V_j)V_j^2 ,$$

where ρ_j is the density in the jet, R_j is the jet's cross section, V_j its velocity, and $\dot{M}_j$ the mass-loss rate in the jet. If we assume

[4] Weliachew and Gottesman (1973) note a pronounced density minimum in the center of M51. Using their data, we find $S_{\rm H\,I} \lesssim 2.8 \times 10^{20}$ atoms cm^{-2}. The H I in the Milky Way is thinnest in the center, with a mean thickness ~ 135 pc (Sanders and Wrixon 1973) in the central 500 parsecs. If we take this as a scale height in M51, $\rho \approx 1$ cm^{-3}.

that the shocks in the bubble are driven by ram pressure from the jet, pressure equilibrium requires (ZDM) that

$$\dot{M}_j V_j = \tfrac{3}{4}\rho_0 r^2 V_s^2 d\Omega ,$$

where ρ_0 is the density in the unshocked disk, r is the distance from the source to the working surface, $d\Omega$ is the solid angle of the jet's opening cone, and V_s is the shock velocity. Based on our estimate of the density in the disk, we take $\rho_0 = 1 \times \mu m_H$ g cm^{-3}, and assume that the working surface is the bow-shaped region seen on the south side of the XNC, which gives $r = 3''.6$ (169 pc), and $d\Omega \approx 0.55$. We assume 185 km s^{-1} for the shock velocity V_s, a value which characterizes the gas motion in the XNC (HWHM) and which gives a model shock spectrum in reasonable agreement with the observed spectrum. We assume that the cross section of the jet is $R_j \approx 12$ pc, a value which is half the radio minor axis of the bubble. Using these values, the two equations can be solved to give $V_j \approx 2.4 \times 10^4$ km s^{-1}, $\dot{M}_j \approx 5.3 \times 10^{-4}\ M_\odot$ yr^{-1}, and $\rho_j \approx 1.4 \times 10^{-3}$ cm^{-3}. For comparison, Bicknell (1984) fits a model of a turbulent low-Mach-number jet propagating through a confining galactic atmosphere to the radio jet in 3C 31 (Fomalont *et al.* 1980, 1983; Strom *et al.* 1983) and derives $E_j \approx 10^{41}$ ergs s^{-1}, $v_j \approx$ 10,000 km s^{-1}, $\dot{M}_j \approx 3 \times 10^{-3}\ M_\odot$ yr^{-1}, and $\rho_j \approx 10^{-4}$ cm^{-3} at a position in the jet 9″ (4.4 kpc) from the nucleus. Because of the uncertainty in our input parameters, the values derived for M51 can only be considered indicative of the jet's characteristics. Nonetheless, it appears that the jet must be moderately relativistic and relatively dense. The mass-loss rate and energy requirements are not very onerous relative to other active nuclei. If the luminosity of the XNC derives from the mechanical energy of a jet caused by critical accretion onto a black hole, the mass of the black hole is $M/M_\odot \approx E_j/1.3 \times 10^{38}$ ergs s$^{-1} \approx 1000$.

ii) *Ejection of Plasmoids*

Arguments presented in the previous section strongly suggest that the ring and XNC are several thousand solar masses of highly filamented gas interacting with the disk. The radio morphologies and physical properties of the relativistic plasmas closely resemble those of the ring-shaped lobes found in the edge-on spiral galaxy NGC 3079 by Duric *et al.* (1983). The pairing of the lobes across the nucleus and along the minor axis of the edge-on galaxy make it almost certain that the lobes, or bubbles, lie out of the plane of the galaxy. Duric *et al.* conclude that the lobes were produced by Parker instabilities or jetlike phenomena. A similar process in M51 could have resulted in the ejection of a pair of bubbles, as described by Smith *et al.* (1983). Evidence for ejection includes the elongation of the nuclear radio source along the line joining the two bubbles and, in particular, the appearance of the XNC. Its leading edge appears to be a working surface for a bubble moving through the interstellar medium (cf. Fig. 5*a*). As previously noted, the spectral index decreases from about -0.7 to -1.4 from the southeast to the northwest edge, which indicates that the southeast edge is where the energetic electrons are being produced.

The ring is foreshortened along the direction toward the nucleus and XNC, as if it were propagating through the interstellar medium in that direction. Its northeast edge is brightest just where it is adjacent to (or overlaps) one of M51's inner spiral arms; this is apparent in Figure 6. The ring appears to be a mature, shell-like source with a fairly constant spectral index of about -0.7. The combination of the geometry and limb brightening suggests that the northern and southern sources originated as bubbles ejected from the nucleus of M51.

IV. SUMMARY

The primary sites of nuclear activity in M51, as measured by optical luminosity, radio luminosity, and line broadening, are *outside* the nucleus. We conclude that interaction of a pair of bubbles with M51's nuclear disk provides a unifying explanation for the bright optical and radio sources. We consider two origins for the bubbles. In the first, a jet entrains gas and, by working against gas in the disk, converts kinetic to thermal energy which drives inflation of the bubbles. The optical and radio emission arise from gas that is compressed and shocked by entrainment in the jet and by expansion of the bubbles. The line broadening results from turbulence in the jet and expansion of the bubbles. Alternatively, the bubbles may be ejected from the nucleus as discrete entities. Evolution proceeds much as with a jet, except that the primary source of mechanical energy is expansion of the bubbles and their motion through the disk. Further observational and theoretical work will be needed to distinguish between the two possibilities. If other active spirals are similar to M51, high-spatial-resolution studies may eventually show that their forbidden-line emission also arises from the interaction of jets or bubbles with the interstellar medium near the nucleus. In the meantime, M51 provides an opportunity to separately study a Seyfert-like nucleus and the effects of the nuclear activity in the surrounding interstellar medium.

H. C. F. is indebted to the Australian National University for a Visiting Fellowship and the hospitality at Stromlo Observatory that allowed completion of this research. We are grateful to M. Dopita for many useful discussions about shock-excited gas and for making the Stromlo radiative shock code available to us. We benefited from discussions with G. Bicknell, J. Norris, and L. Cowie. C. Sarazin kindly made his M51 X-ray data available to us in advance of publication. We are grateful to D. Jenner and H. Epps for help in acquiring the Lick data. Robin Ciardullo provided valuable help in analyzing the ICCD data.

REFERENCES

Abell, G. O., and Margon, B. 1979, *Nature*, **279**, 701.
Arnett, W. 1971, *Ap. J.*, **166**, 153.
Baars, J. W. M., Genzel, R., Pauliny-Toth, I. I. K., and Witzel, A. 1977, *Astr. Ap.*, **61**, 99.
Baldwin, J. A., Phillips, M. M., and Terlevich, R. 1981, *Pub. A.S.P.*, **93**, 5.
Bicknell, G. V. 1984, preprint.
Blair, W. P., Kirshner, R. P., and Chevalier, R. A. 1981, *Ap. J.*, **247**, 879.
Blandford, R. D., and Rees, M. J. 1974, *M.N.R.A.S.*, **169**, 395.
Burbidge, E. M., and Burbidge, G. R. 1964, *Ap. J.*, **140**, 1445.
Condon, J. J., Condon, M. A., Gisler, G., and Puschell, J. J. 1982, *Ap. J.*, **252**, 102.
Dopita, M. A. 1981, in *Supernovae: A Survey of Current Research* (Proc. NATO Advanced Study Institute), ed. M. J. Rees and R. J. Stoneham (Dordrecht: Reidel), p. 483.
Dopita, M. A., Binette, L., and Tuohy, I. R. 1984, *Ap. J.*, **282**, 142.
Dopita, M. A., Mathewson, D. S., and Ford, V. L. 1977, *Ap. J.*, **214**, 179.
Duric, N., Seaquist, E. R., Crane, P. C., Bignell, R. C., and Davies, L. E. 1983, *Ap. J. (Letters)*, **273**, L11.
Ekers, R. D. 1980, *Highlights Astr.*, **5**, 143.
Fomalont, E. B., Bridle, A. H., Willis, A. G., and Perley, R. A. 1980, *Ap. J.*, **237**, 418.

Fomalont, E. B., Fanti, R., Parma, P., and Ekers, R. D. 1983, *Astr. Ap.*, **122**, 305.
Fosbury, R. A. E., Mebold, V., Goss, W. M., and Dopita, M. A. 1978, *Astr. Ap.*, **183**, 549.
Geldzahler, B. J., Pauls, T., and Salter, C. J. 1980, *Astr. Ap.*, **84**, 237.
Goad, J. W., De Veny, J. B., and Goad, L. E. 1979, *Ap. J. Suppl.*, **39**, 439 (GDVG).
Gower, A. C., Gregory, P. C., Hutchings, J. B., and Unruh, W. G. 1982, *Ap. J.*, **262**, 478.
Halpern, J. P., and Steiner, J. E. 1983, *Ap. J. (Letters)*, **269**, L37.
Heckman, T. M. 1980, *Astr. Ap.*, **87**, 152.
Hummel, E. 1980, *Astr. Ap. Suppl.*, **41**, 151.
Jenner, D. C., Ford, H. C., and Jacoby, G. H. 1979, *Ap. J.*, **227**, 391.
Keel, W. C., and Miller, J. S. 1983, *Ap. J. (Letters)*, **266**, L89.
Koski, A. T., and Osterbrock, D. E. 1976, *Ap. J. (Letters)*, **203**, L49.
Kunth, D., and Sargent, W. L. W. 1981, *Astr. Ap.*, **101**, L5.
Margon, B., Ford, H. C., Katz, J. I., Kwitter, K. B., Ulrich, R. K., Stone, R. P. S., and Klemola, A. 1979, *Ap. J. (Letters)*, **230**, L41.
McCall, M. L. 1984, *M.N.R.A.S.*, **208**, 253.
Mendoza, C. 1983, in *IAU Symp. 103, Planetary Nebulae*, ed. D. R. Flower (Dordrecht: Reidel), p. 143.
Miley, G. 1980, *Ann. Rev. Astr. Ap.*, **18**, 165.
Miller, J. S., and Mathews, W. G. 1972, *Ap. J.*, **172**, 593.
Milne, D. 1979, *Australian J. Phys.*, **32**, 83.
Moffet, A. T. 1975, in *Stars and Stellar Systems*, Vol. **9**, *Galaxies and the Universe*, ed. A. Sandage, M. Sandage, and J. Kristian (Chicago: University of Chicago Press), p. 211.
Neugebauer, G., *et al.* 1980, *Ap. J.*, **238**, 502.
Norman, G., and Silk, J. 1983, *Ap. J.*, **266**, 502.
Oke, J. B. 1969, *Pub. A.S.P.*, **81**, 11.
Osterbrock, D. E., and Cohen, R. D. 1982, *Ap. J.*, **261**, 64.
Osterbrock, D. E., and Miller, J. S. 1975, *Ap. J.*, **197**, 535.
Parker, R. A. R. 1978, *Ap. J.*, **224**, 873.
Peimbert, M. 1968, *Ap. J.*, **154**, 33.
Peimbert, M., and Torres-Peimbert, S. 1983, in *IAU Symp. 103, Planetary Nebulae*, ed. D. R. Flower (Dordrecht: Reidel), p. 233.
Peimbert, M., Torres-Peimbert, S., and Rayo, J. F. 1978, *Ap. J.*, **220**, 516.
Raymond, J. C. 1979, *Ap. J. Suppl.*, **39**, 1.
Robinson, L. B., and Wampler, E. J. 1972, *Pub. A.S.P.*, **84**, 161.
———. 1973, in *Astronomical Observations with Television Type Sensors*, ed. J. W. Glaspey and G. A. H. Walker (Vancouver: University of British Columbia Press), p. 69.
Rose, J. A., and Cecil, G. 1983, *Ap. J.*, **266**, 531 (RC).
Rose, J. A., and Searle, L. 1982, *Ap. J.*, **253**, 556 (RS).
Rose, J. A., and Tripicco, M. J. 1984, preprint.
Sandage, A. R. 1971, in *Nuclei of Galaxies*, ed. D. J. K. O'Connell (Amsterdam: North Holland), p. 271.
Sandage, A. R., and Tammann, G. A. 1974, *Ap. J.*, **194**, 559.
Sanders, R. H., and Wrixon, G. T. 1975, *Astr. Ap.*, **26**, 365.
Sarazin, C. 1983, private communication.
Schwab, F. 1980, *Proc. Soc. Photo-Optical Instrumentation Engineers*, **231**, 18.
Searle, L. 1971, *Ap. J.*, **168**, 327.
Segalovitz, A. 1976, *Astr. Ap.*, **52**, 167.
Shields, G. A. 1974, *Ap. J.*, **193**, 335.
Shull, J. M., and McKee, C. F. 1979, *Ap. J.*, **227**, 131.
Smith, H. E. 1975, *Ap. J.*, **199**, 591.
Smith, M. D., Smarr, L. Norman, M. L., and Wilson, J. R. 1983, *Ap. J.*, **264**, 432.
Spencer, J. H., and Burke, B. F. 1972, *Ap. J. (Letters)*, **176**, L101.
Strom, R. G., Fanti, R., Parma, P., and Ekers, R. D. 1983, *Astr. Ap.*, **122**, 305.
Torres-Peimbert, S., Peimbert, M., and Daltabuit, E. 1980, *Ap. J.*, **238**, 133.
Turnrose, B. E. 1976, *Ap. J.*, **210**, 33.
Ulvestad, J. S., and Wilson, A. S. 1983, *Ap. J. (Letters)*, **264**, L7.
Ulvestad, J. S., Wilson, A. S., and Sramek, R. A. 1981, *Ap. J.*, **247**, 419.
van den Bergh, S. 1979, *IAU Circ.*, No. 3393.
van der Hulst, J. M. 1980, *Highlights Astr.*, **5**, 177.
van der Hulst, J. M., Crane, P. C., and Keel, W. C. 1981, *A.J.*, **86**, 1175.
van der Hulst, J. M., Crane, P. C., Kennicutt, R., and Allen, R. 1985, in preparation.
Weiler, K. A., Sramek, R. A., van der Hulst, J. M., and Panagia, N. 1983, in *IAU Symp. 101, Supernova Remnants and Their X-Ray Emission*, ed. J. Danziger and P. Gorenstein (Dordrecht: Reidel), p. 171.
Weliachew, L., and Gottesman, S. T. 1973, *Astr. Ap.*, **24**, 59.
Wilson, A. S., and Ulvestad, J. S. 1982, *Ap. J.*, **263**, 576 (WU).
———. 1983, *Ap. J.*, **275**, 8.
Wilson, A. S., and Willis, A. G. 1980, *Ap. J.*, **240**, 429.
Zealy, W. J., Dopita, M. A., and Malin, D. F. 1980, *M.N.R.A.S.*, **192**, 731 (ZDM).

PATRICK C. CRANE: NRAO, P. O. Box O, Socorro, NM 87801

HOLLAND C. FORD: ST ScI, Homewood Campus, Baltimore, MD 21218

GEORGE C. JACOBY: KPNO, P. O. Box 26732, Tucson, AZ 85726

DAVID G. LAWRIE: Dept. of Astronomy, Ohio State University, Columbus, OH 43210

JAN MATHIJS VAN DER HULST: Netherlands Foundation for Radio Astronomy, Radio Sterrenwacht Westerbork, 9433 TA Zwiggelte, The Netherlands